Article

Current Biology

Growth and tension in explosive fruit

Graphical abstract

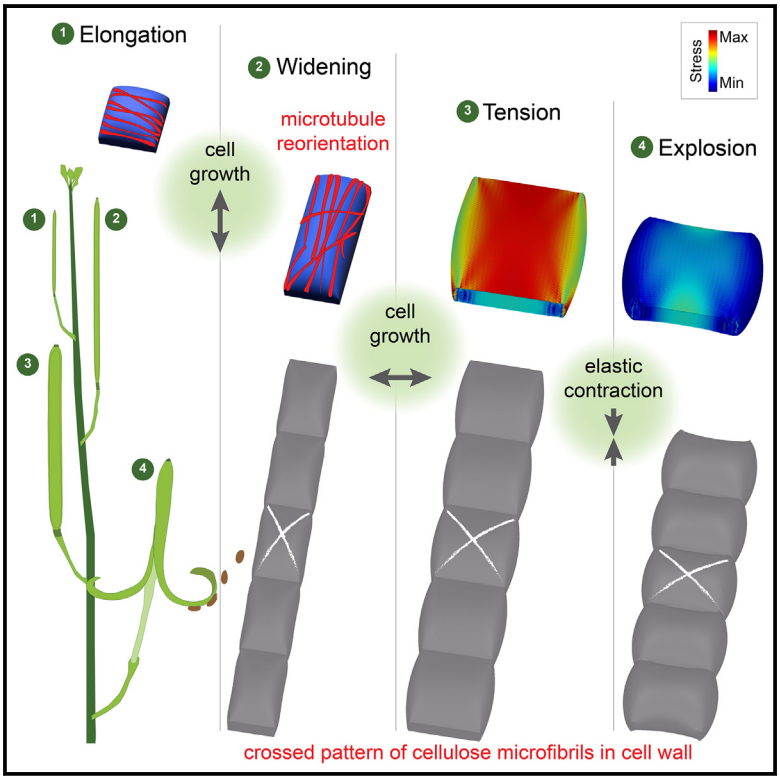

Highlights

- Growth generates contractility and pulling force in the fruit exocarp
- Switch in microtubule orientation underlies change in cellular growth patterns
- Crossed pattern of cellulose microfibrils enhances contraction of growing cells
- Multi-layered growth framework used to model cross-lamellate cell walls

Authors

Gabriella Mosca, Ryan C. Eng, Milad Adibi, ..., Gaby Weber, Richard S. Smith, Angela Hay

Correspondence

hay@mpipz.mpg.de

In brief

How growth—a stress relaxation process—produces tension in exploding seed pods is puzzling. Mosca et al. find that a specific pattern of cell expansion, regulated by microtubule-dependent cellulose deposition, leads to contractile tension. Growth also has an active role in increasing tension on cellulose fibers in a cross-lamellate cell wall.

Mosca et al., 2024, Current Biology *34*, 1–13
March 11, 2024
https://doi.org/10.1016/j.cub.2024.01.059

CellPress

Please cite this article in press as: Mosca et al., Growth and tension in explosive fruit, Current Biology (2024), https://doi.org/10.1016/j.cub.2024.01.059

Current Biology

CellPress
OPEN ACCESS

Article

Growth and tension in explosive fruit

Gabriella Mosca,[1,2,4,8] Ryan C. Eng,[1,8] Milad Adibi,[1,5,8] Saiko Yoshida,[1,6] Brendan Lane,[1,3] Leona Bergheim,[1,7] Gaby Weber,[1] Richard S. Smith,[1,3] and Angela Hay[1,9,*]

[1]Max Planck Institute for Plant Breeding Research, Carl-von-Linné-Weg 10, 50829 Köln, Germany
[2]Technical University of Munich, 85748 Garching b. Munich, Germany
[3]John Innes Centre, Norwich NR4 7UH, UK
[4]Present address: ZMBP, University of Tübingen, Auf der Morgenstelle 32, 72076 Tübingen, Germany
[5]Present address: ETH, Otto-Stern-Weg 7, 8093/University of Zurich, Winterthurerstrasse 190, 8057 Zurich, Switzerland
[6]Present address: University of Bern, Altenbergrain 21, 3013 Bern, Switzerland
[7]Present address: HBRS, University of Applied Sciences, 53757 Sankt Augustin, Germany
[8]These authors contributed equally
[9]Lead contact
*Correspondence: hay@mpipz.mpg.de
https://doi.org/10.1016/j.cub.2024.01.059

SUMMARY

Exploding seed pods of the common weed *Cardamine hirsuta* have the remarkable ability to launch seeds far from the plant. The energy for this explosion comes from tension that builds up in the fruit valves. Above a critical threshold, the fruit fractures along its dehiscence zone and the two valves coil explosively, ejecting the seeds. A common mechanism to generate tension is drying, causing tissues to shrink. However, this does not happen in *C. hirsuta* fruit. Instead, tension is produced by active contraction of growing exocarp cells in the outer layer of the fruit valves. Exactly how growth causes the exocarp tissue to contract and generate pulling force is unknown. Here we show that the reorientation of microtubules in the exocarp cell cortex changes the orientation of cellulose microfibrils in the cell wall and the consequent cellular growth pattern. We used mechanical modeling to show how tension emerges through growth due to the highly anisotropic orientation of load-bearing cellulose microfibrils and their effect on cell shape. By explicitly defining the cell wall as multi-layered in our model, we discovered that a cross-lamellate pattern of cellulose microfibrils further enhances the developing tension in growing cells. Therefore, the interplay of cell wall properties with turgor-driven growth enables the fruit exocarp to generate sufficient tension to power explosive seed dispersal.

INTRODUCTION

Plants have evolved a multitude of different ways to disperse their seeds. Many of these dispersal structures have intriguing mechanical design features. For example, the pappus of the common dandelion has many closely spaced bristles, designed to generate a vortex air flow that optimizes the dispersal of seeds by wind.[1] Exploding seed pods, on the other hand, harness their own power to launch their seeds far from the plant. *Cardamine hirsuta* is a relative of the model plant *Arabidopsis thaliana*, but unlike *A. thaliana*, its seed pods explode. The elongated fruit of both species look very similar, comprising two valves that encase the seeds. In *C. hirsuta*, these valves coil rapidly outward to launch the seeds at speeds greater than 10 m/s.[2] This rapid coiling relies on the differential contraction of valve tissues. Previous work showed that the outer exocarp cell layer of each valve actively contracts its reference length.[2] In contrast, the inner endocarp *b* cell layer of each valve is stiffened by a phenolic polymer called lignin that resists contraction.[3] Tension builds while the elongated valves are physically attached to the rest of the fruit. When structural elements of the fruit valves fail above a critical threshold, the valves rapidly coil to accommodate both the intrinsic contraction of the outer exocarp layer and the resistance to it from the inner lignified layer. It is crucial for the explosive mechanism that a substantial amount of tension develops in the exocarp cell layer, as this is linked to the velocity of seed launch.

Importantly, *C. hirsuta* fruit are characterized by their ability to explode without drying. This distinguishes them from many other explosive fruits that generate tension through the differential shrinkage of drying tissues. The active contraction found in *C. hirsuta* fruit is a consequence of how exocarp cell shape deforms in response to the innate hydrostatic pressure found in plant cells called turgor.[2] Active osmoregulation alters turgor pressure and drives the swelling and shrinking of cells. This mechanism is used, for example, in stomatal guard cells to open and close the stomatal pore or in the specialized joint structures of Mimosa leaves to actuate leaf folding.[4,5] However, the contraction of *C. hirsuta* fruit exocarp cells is not associated with a change in turgor pressure,[2] leaving open the question of how tension develops in the elongated fruit valves.

Turgor pressure is the major driving force behind expansive cell growth in plants. Plant cells are encased by a rigid yet malleable cell wall that functions to counter the large amount of turgor pressure found within a cell. This mechanical

Please cite this article in press as: Mosca et al., Growth and tension in explosive fruit, Current Biology (2024), https://doi.org/10.1016/j.cub.2024.01.059

equilibrium can be turned into expansive growth if the cell wall is stretched beyond a certain threshold. This stretch induced by turgor, combined with active loosening of the cell wall,[6] leads to irreversible expansion. Specifically, the relaxation of cell wall stress by loosening generates a slight reduction in water potential that allows cells to take up water and expand.[7] The growing cell wall is maintained by reinforcement with new wall synthesis, and this continuous loop is reiterated, resulting in expansive growth.[8,9] In this way, the precise interplay between turgor pressure, cell wall loosening, and synthesis determines the growth of plant cells.

The main load-bearing components of the cell wall are cellulose microfibrils, each made up of many β-(1→4)-D-glucan polysaccharide chains, typically packed into a crystalline array. Cellulose microfibrils act as biological steel cables that resist being stretched.[9] Since growth is restricted in the direction of aligned microfibrils, cells preferentially grow in the orthogonal direction. Cellulose microfibrils are synthesized by a heteromeric enzymatic complex composed of cellulose synthase subunits (CESAs) that are localized at the plasma membrane.[10] During cellulose biosynthesis, CESAs extrude microfibrils into the cell wall, which in turn propels the movement of the cellulose synthase complex within the plasma membrane. CESA motility is linear and is usually guided by the cortical microtubule (CMT) cytoskeleton,[11,12] resulting in cellulose microfibrils that mirror the orientation of microtubules. Aligned CESA trajectories can also be observed in microtubule-free domains, guided, for example, by existing cellulose microfibrils when microtubule guidance is temporarily lost.[13,14] Thus, CMTs typically determine cellulose microfibril alignment, which can then influence the direction of cellular growth and consequently cell shape.[15,16]

Here, we discovered that fruit exocarp cells acquire the ability to contract and generate pulling force through the dynamics of growth. However, since growth is a process that relaxes stress in the cell wall, it was unclear how growth could generate contractile tension. To address this problem, we used a combination of computational modeling, live-cell confocal imaging, and microtubule perturbations. We found that a developmental switch in microtubule orientation is critical to reorient cellulose microfibrils and change cellular growth patterns, and consequently cell shape, in the fruit exocarp. Mechanical modeling shows how growth leads to cell contraction via the effects of aligned cellulose microfibrils and cell geometry. By designing a multi-layered modeling framework, we found that a cross-lamellate pattern of cellulose microfibrils can further enhance the active contraction of growing exocarp cells.

RESULTS

Cell shape, anisotropy, and turgor-driven contraction

The elongated seed pods of *A. thaliana* and *C. hirsuta* look very similar despite their striking difference in seed dispersal (Figure 1A). Yet underlying these similar organ shapes are very different cell shapes. Exocarp cells, which comprise the epidermal layer of the fruit valve, have an elongated shape in *A. thaliana*, described by high aspect ratios with considerable variation (Figures 1B and 1D). These same cells are uniformly square in *C. hirsuta* (Figures 1B and 1D). Exocarp cells grow larger by cell expansion without division during post-fertilization development of the fruit in both *A. thaliana* and *C. hirsuta*.[17,18] Turgor pressure in plant cells exerts mechanical tension on the cell wall, which generates in-plane stresses in the wall to resist it. This in-plane stress varies with the size and shape of the cell and increases when cells become large in both length and width, causing cell walls to bulge excessively.[19] In contrast to the elongated shape of exocarp cells in *A. thaliana* (Figure 1D), the outer and inner faces of exocarp cells in *C. hirsuta* have a large, square shape (Figure 1D), suggesting that these cell walls could bulge out in response to turgor and experience significant stress. To describe the patterns of exocarp cell expansion during *A. thaliana* and *C. hirsuta* fruit development, we measured cell area and the area of the largest empty circle (LEC) that fits inside a cell contour (Figure 1D). LEC area has been used previously as a proxy for the magnitude of mechanical stress that accumulates in the center of a cell face.[19] We found that LEC area remained relatively constant as exocarp cell area increased in *A. thaliana* (Figure 1C), indicating that stress is likely to be minimized by this pattern of cell expansion. However, in *C. hirsuta*, LEC area increased as cell area increased (Figure 1C), predicting a large increase in stress as cells expand. In fact, the LEC area becomes twice as large in *C. hirsuta* compared to *A. thaliana* cells, even though cell size is much larger in *A. thaliana* (Figures 1C and 1D). By analyzing *C. hirsuta* exocarp cells separately at early versus late stages of fruit development, we found that LEC area increased together with cell area only during later stages, when cells expanded in width to acquire a square shape (Figures 1D and 1E). Therefore, we predict that the pattern of exocarp cell expansion during later stages of *C. hirsuta* fruit development leads to high mechanical stress in the cell wall.

When cells are plasmolyzed during osmotic treatments, the amount of shrinkage and its directions can be used to estimate cell wall stiffness and anisotropy. Previously, we showed that a strongly anisotropic cell wall, combined with the cell geometry seen in later-stage *C. hirsuta* exocarp cells, will cause cells to contract in length and expand in depth and width in response to turgor pressure.[2] To understand exocarp cell mechanics, and how they change during *C. hirsuta* fruit development, we performed osmotic treatments on valves at early versus late stages of fruit development (Figures 2A and 2B). We quantified exocarp cell surface dimensions of plasmolyzed versus turgid cells in plants containing a *p35S::GFP:TUA6* microtubule reporter,[2] using the depolymerization of CMTs as an indicator of plasmolysis.[20] In elongating fruit at early stages of development (stage 15), exocarp cells responded to increased turgor by expanding in length (+9.4% ± 0.3%; mean ± SEM; Figures 2A and 2C) and contracting slightly in width (–4.2% ± 0.4%) (Figure S1). However, during later fruit stages (stage 17b), cells contracted in length in response to increased turgor (–14% ± 0.3%; Figures 2B and 2C) and expanded in width (+14.9% ± 0.2%). Thus, exocarp cells switched their response to turgor during fruit development, from length expansion to length contraction (Figure 2C). These findings suggest that cell wall anisotropy changes during development, such that mature exocarp cells contract in length in response to turgor.

We reproduced this turgor-driven contraction of mature exocarp cells using finite element method (FEM) simulations both here (Figure 2D) and previously.[2] We found that the contraction in cell length results from the combined action of turgor

Please cite this article in press as: Mosca et al., Growth and tension in explosive fruit, Current Biology (2024), https://doi.org/10.1016/j.cub.2024.01.059

CellPress
OPEN ACCESS

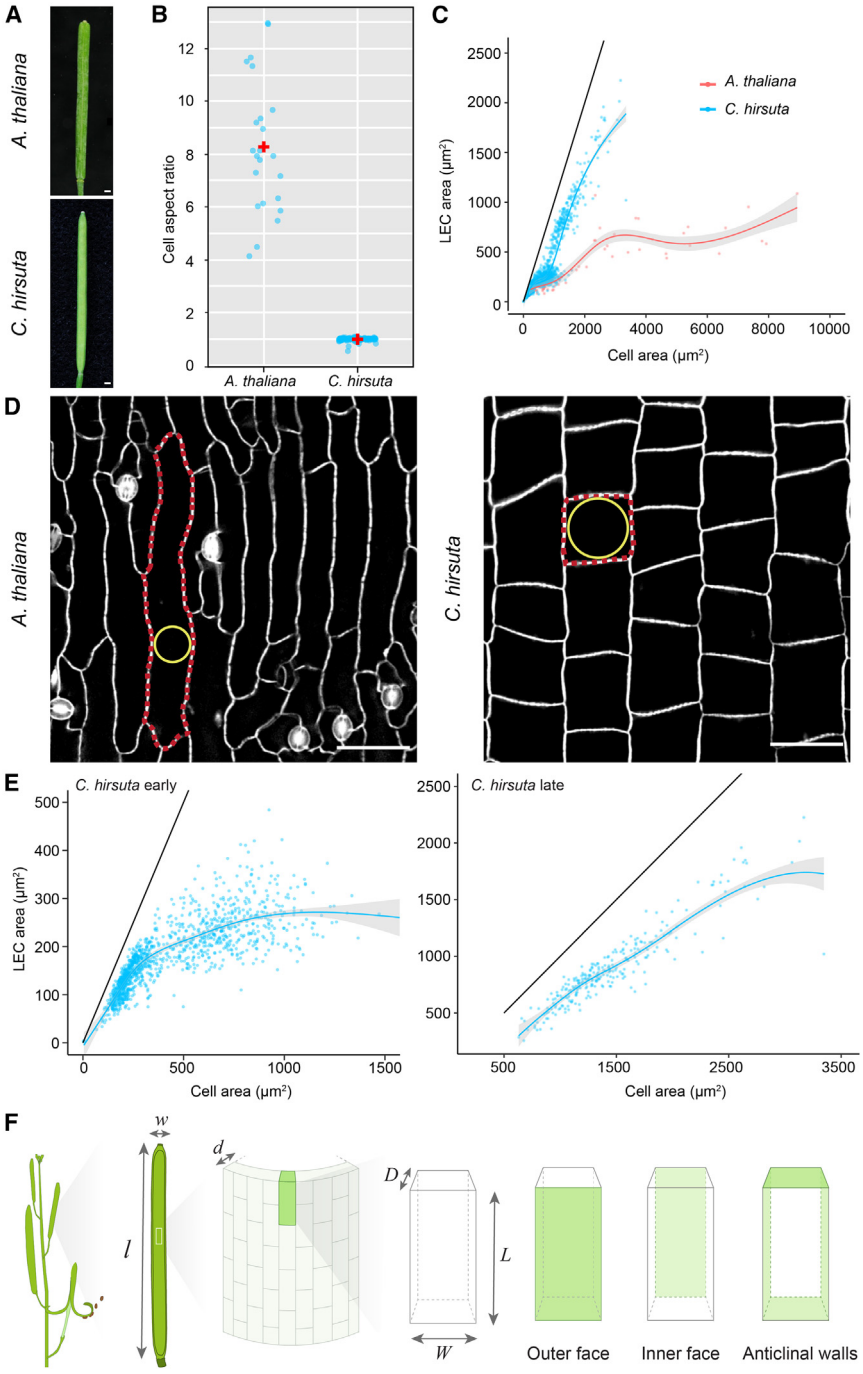

Figure 1. Different patterns of cell expansion underlie similar fruit shapes

(A) Mature fruits of *A. thaliana* and *C. hirsuta*.

(B) Exocarp cell aspect ratio (ratio of cell length to width) in mature *A. thaliana* and *C. hirsuta* fruits. n = 145 cells.

(C) Exocarp cell area (x axis) versus the largest empty circle area (LEC, y axis) in stage 15–17b fruit of *A. thaliana* (red) and *C. hirsuta* (blue). Smooth curves fitted and 95% confidence intervals (gray) shown; black line indicates perfect circle. n = 1,568 cells.

(D) Exocarp cells in mature fruit of *A. thaliana* and *C. hirsuta*, stained with propidium iodide; representative cell outlined (red) and largest empty circle that fits inside (LEC, yellow) indicated in each image.

(E) *C. hirsuta* exocarp cell area (x axis) versus LEC (y axis) in early fruit (stage 15–17a, n = 1,220 cells) and late fruit (stage 17b, n = 258 cells). Smooth curves fitted and 95% confidence intervals (gray) shown; black line indicates perfect circle.

(F) Explanatory cartoon describing exocarp cell length (*L*), width (*W*), and depth (*D*) in relation to the length (*l*), width (*w*), and depth (*d*) of the fruit valve. From left: fruit attached to the plant stem, valve attached to fruit with directions *l* and *w* indicated, zoom-in of boxed region of the valve exocarp with direction *d* indicated, and zoom-in of exocarp cell shown in green with directions *L*, *W*, and *D* indicated. Description of exocarp cell walls: outer face facing outside of fruit; inner face facing inside of fruit and anticlinal walls.

Scale bars, 1 mm (A) and 50 µm (D).

pressure, which pushes the cell wall to expand, and high material anisotropy in the direction parallel to the cell length. This causes the cell wall to resist stretch in the length direction. When pressurized, these cells expand in width and depth and increase their curvature much more in the length direction, causing the large cell faces to bulge out (Figure 2D). In this way, the straight-line distance along the cell length contracts (Figure 2D). We used further FEM simulations to investigate whether expansion in cell width, which we observed during later stages of *C. hirsuta* fruit development (Figures 1D and 1E), could be instrumental in building contractile force when combined with material anisotropy of the cell wall. Using inflation simulations with MorphoMechanX software (https://www.morphomechanx.org/), we explored the effects of increasing cell width for a fixed combination of anisotropic material properties and pressure[2] (Table S1). All cell files were generated with the same cell length (50 µm) and depth (10 µm), while cell width was progressively increased in each simulation (Figure 2E). For each cell width, a file of non-pressurized cells with ends fixed in the y-direction were inflated to 0.7 MPa. When we computed the stretch ratio between the length of the cell file with free versus fixed ends (Figure S2B), we found that increasing cell width enhanced the length contraction (Figure 2E). The stretch ratio decreased from 0.98 to 0.78 as cell width increased from 10 to 100 µm, although it started to plateau beyond a cell width of 50 µm (Figure 2E). Mechanical stress increased in the center of the surface walls as cell width increased from 10 to 50 µm (Figure 2F), particularly the longitudinal stress component that is directly connected to the pulling force (Figure S2C). This is in agreement with the increased stress predicted by LEC area measurements of mature exocarp cells

Please cite this article in press as: Mosca et al., Growth and tension in explosive fruit, Current Biology (2024), https://doi.org/10.1016/j.cub.2024.01.059

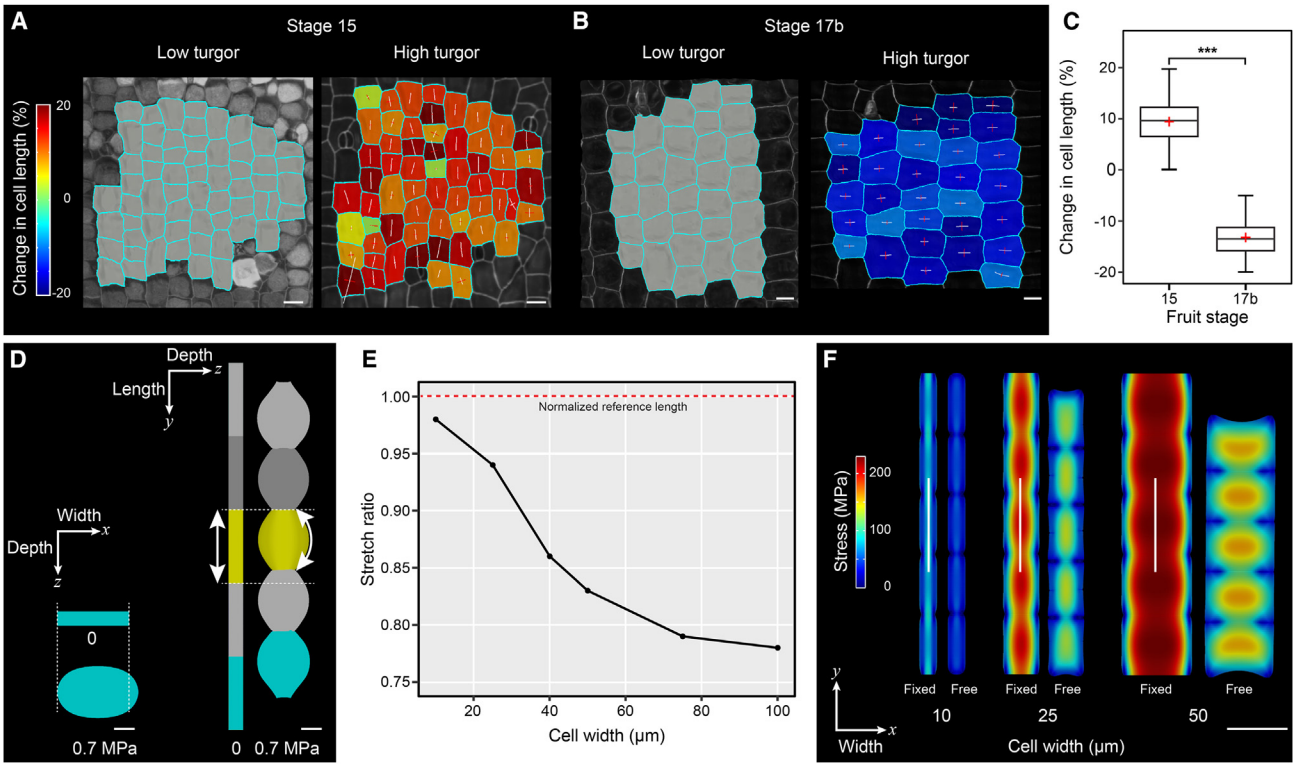

Figure 2. Contraction of exocarp cell length is determined by cell wall anisotropy and enhanced by cell width

(A and B) Osmotic treatment of (A) stage 15 and (B) stage 17b *C. hirsuta* fruit. Heatmaps show percentage change in exocarp cell length, relative to the long axis of the fruit, in high turgor pressure (pure water) relative to low turgor pressure (1 M salt). Lines indicate expansion (white) or shrinkage (red) of cell dimensions.

(C) Boxplot of change in exocarp cell length showing mean (red cross) for stage 15 (n = 165 cells from 3 fruit) and stage 17b (n = 227 cells from 6 fruit) and significant difference at ***$p < 0.001$ using a Wilcoxon signed-rank test.

(D–F) FEM simulations in MorphoMechanX of cells inflated from 0 to 0.7 MPa.

(D) Material anisotropy is specified in the length direction, indicated by double-headed arrow, in 50 × 50 × 10 μm (length × width × depth) cells. Inflated cells expand in width (cyan cell viewed end on, left) and contract in length (yellow cell viewed side on). Dashed lines indicate initial cell dimensions before inflation. High anisotropy in the length direction causes the cells to bulge in depth upon inflation (curvature of double-headed arrow).

(E) Plot of stretch ratio (y axis), measured along the length of inflated cell file when ends are free versus fixed, in six different simulations where cell width (x axis) progressively increases.

(F) Length contraction compared between three simulations with different cell widths (10, 25, and 50 μm). For each cell width, trace of Cauchy stress tensor (MPa) is compared when the inflated cell file ends are fixed versus free. White lines indicate direction of material anisotropy in each simulation. Coordinates show the orientation of cell depth (*z*), width (*x*), and length (*y*) relative to the fruit (D and F).

Scale bars, 20 μm (A and B), 10 μm (D), and 50 μm (F).

See also Figures S1 and S2.

that expanded in width to acquire their final, square shape (Figures 1D and 1E). A reduction in wall stress was associated with contraction of the cell file after the ends were released in the simulations (Figure 2F). Therefore, these inflation simulations indicate that as cells become wider, they can contract more in length.

The relatively shallow depth of mature exocarp cells is also important for length contraction. For example, increasing cell depth from 10 to 50 μm elevated the stretch ratio from 0.83 to 0.92 (Figure S2D). These cells accumulated high mechanical stress in the center of not only inner and outer cell faces, but also anticlinal walls (Figure S2D). This created conflicts during the minimization of cell wall mechanical energy, which reduced the amount of length contraction in the simulation (Figure S2D). In summary, cell shape plays an important role in amplifying exocarp cell contraction.

Orientation of cortical microtubules and CESA3 trajectories predict growth direction

Our results from osmotic treatments and model simulations show that wider cells can contract more when inflated. To understand how exocarp cells grow into this more optimal shape, we quantified growth at cellular resolution during *C. hirsuta* fruit development. Specifically, we used time-lapse confocal microscopy to image the exocarp of fruit expressing a CMT marker (*p35S::GFP:TUA6*[2]) and analyzed these confocal stacks using MorphoGraphX.[21] From an initial time series, we identified a switch in anisotropy (Figure S2E). To capture this transition, we began each of our time series replicates in 7-mm-long fruit, once cell division had ceased in the exocarp, and imaged three subsequent time points (48 h, 96 h, and 8 days). We identified two phases of highly anisotropic growth during the first 48 h and the last 96 h, separated by

Please cite this article in press as: Mosca et al., Growth and tension in explosive fruit, Current Biology (2024), https://doi.org/10.1016/j.cub.2024.01.059

CellPress
OPEN ACCESS

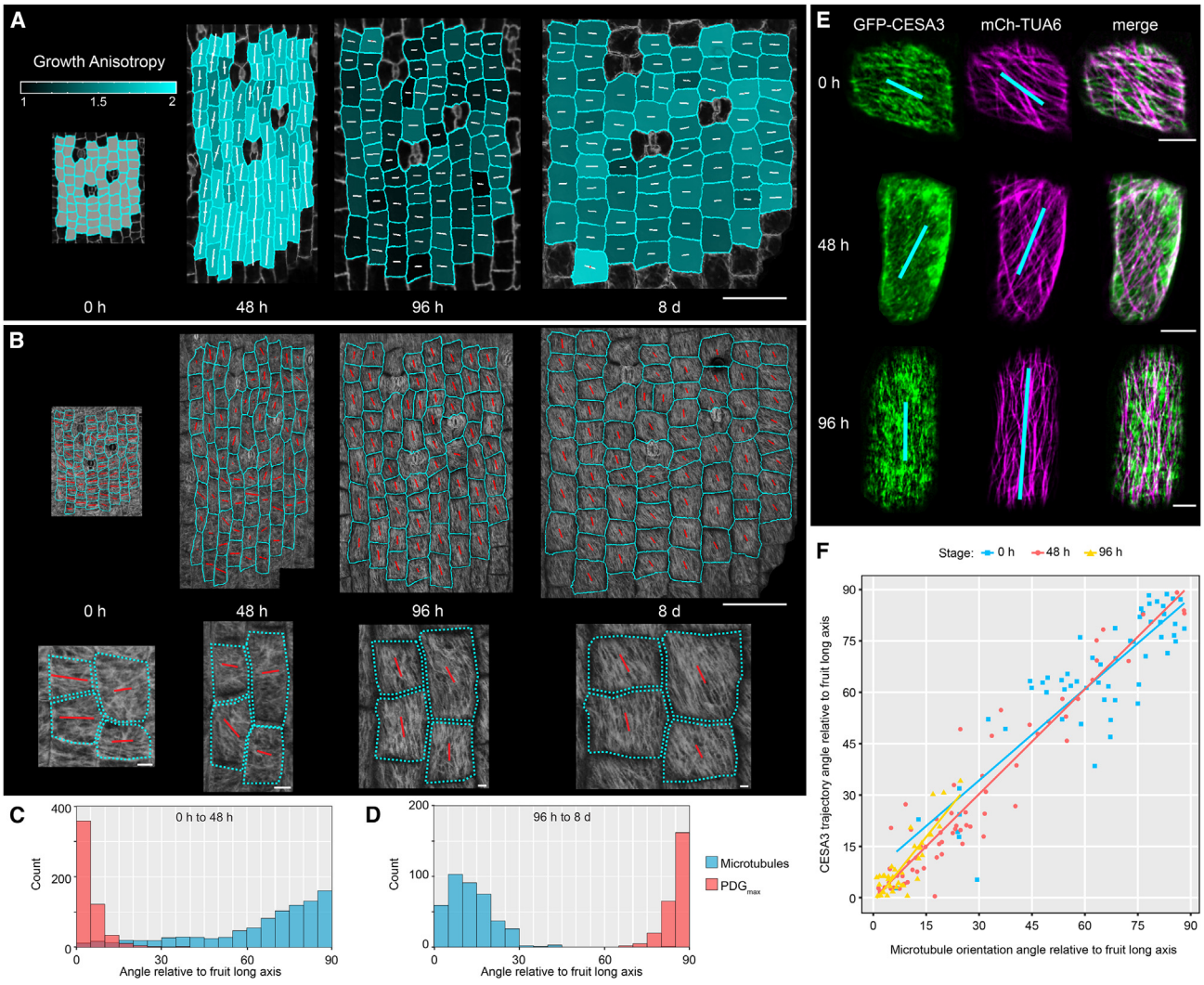

Figure 3. Orientation of cortical microtubules and CESA3 trajectories predict directional growth in fruit exocarp cells

(A and B) Time-lapse confocal imaging of *C. hirsuta* exocarp cells during 8 days of fruit development starting with 7-mm-long fruit at 0 h. Growth anisotropy (ratio of PDG_{max} to PDG_{min}) between consecutive time points shown as heatmaps on second time point (A). White lines in each cell indicate the magnitude and direction of PDG_{max} (longer lines) and PDG_{min} (shorter lines). CMT marker GFP-TUA6 at 0, 48, and 96 h and 8 days (B). Orientation and magnitude of CMT arrays calculated with FibrilTool and shown as direction and length of red lines; cells outlined in cyan; magnified views shown below.

(C and D) Histograms showing the principal direction of growth (PDG_{max}, red) and CMT orientation (blue) as angles relative to the long axis of the fruit at 0–48 h (C) and 96 h–8 days (D). PDG_{max} calculated between consecutive time points as indicated, n = 535 (C) and 253 cells (D). CMT orientation calculated at 0 h, n = 934 cells (C), and 96 h, n = 398 cells (D).

(E) Co-localization of GFP-CESA3 and mCherry-TUA6 in exocarp cells of *C. hirsuta* fruit at 0, 48, and 96 h, starting with 7-mm-long fruit at 0 h. Average projections of confocal time-lapse movies (Videos S1, S2, and S3) showing GFP-CESA3 (green), mCherry-TUA6 (magenta), and merge of both channels. Orientation and magnitude of CESA3 trajectories and CMT arrays calculated with FibrilTool and shown as direction and length of blue lines.

(F) Scatterplot showing correlation between the angles of GFP-CESA3 trajectories and CMT orientations in fruit exocarp cells relative to the long axis of the fruit; dots indicate individual cells and lines indicate linear regressions at 0 h (blue; $r = 0.87$, $p < 4.9e{-}19$, n = 58 cells), 48 h (red; $r = 0.95$, $p < 4.15e{-}34$, n = 65 cells), and 96 h (yellow; $r = 0.86$, $p < 9.87e{-}11$, n = 34 cells).

Scale bars, 100 μm (A and B) and 5 μm (B [magnified] and E).

See also Figure S2 and Videos S1, S2, and S3.

a period of more isotropic growth between 48 and 96 h (Figure 3A). The largest amount of growth occurred during the first 48 h (Figures 3A, S4D, and S4E). Growth anisotropy was parallel to the long axis of the fruit from 0 to 48 h and then switched to perpendicular (Figure 3A). Through this pattern of anisotropic growth, exocarp cells initially expand by elongating and then switch to growth in the width direction to acquire their final, square shape.

Cells grow principally in the direction orthogonal to aligned cellulose microfibrils in the cell wall. Since the alignment of microfibrils usually mirrors the orientation of CMTs,[11] we investigated to what extent the growth anisotropy of exocarp cells

Please cite this article in press as: Mosca et al., Growth and tension in explosive fruit, Current Biology (2024), https://doi.org/10.1016/j.cub.2024.01.059

was predicted by CMT orientation. The initial alignment of CMTs was perpendicular to the long axis of the fruit (0 h; Figure 3B), giving a distribution of CMT angles skewed toward 90° (Figure 3C). This CMT alignment was a good predictor of the principal direction of cellular growth (PDG_{max}) in the orthogonal direction during the subsequent 48 h (Figure 3C). CMT arrays began to re-align and had no principal orientation by 48 h (Figure 3B), prior to the subsequent period of more isotropic growth (48–96 h; Figures 3A and S2F–S2H). By 96 h, CMT arrays were well aligned and their orientation had switched to parallel to the long axis of the fruit (96 h; Figure 3B), resulting in a distribution of CMT angles skewed toward 0° (Figure 3D). This new CMT alignment accurately predicted a switch in PDG_{max} to the orthogonal direction during the subsequent 96 h (Figure 3D). This CMT alignment parallel to the fruit long axis was maintained through to the last time point at 8 days (Figure 3B). Therefore, CMT orientation is highly predictive of growth anisotropy in the fruit exocarp.

However, CMT orientation is only a proxy for cellulose microfibril alignment. Therefore, we analyzed the orientation of cellulose synthase 3 (CESA3) trajectories during exocarp cell growth. Specifically, we visualized *pCESA3::GFP:CESA3* together with *pUbi10::mCherry:TUA6* in exocarp cells of *C. hirsuta* fruit during 96 h of development (Videos S1, S2, and S3). We measured the orientation of CMTs and CESA3 trajectories per cell in average projections of these time-lapse movies (Figure 3E). The orientation of CMTs and CESA3 trajectories were highly correlated at each time point (Figure 3F) and showed the same switch from transverse to longitudinal orientations that we observed for CMTs previously (Figures 3B–3E). Thus, CMT orientation matches the orientation in which new cellulose microfibrils are synthesized in exocarp cells of *C. hirsuta* fruit. Consequently, CMT realignment in mature exocarp cells contributes to a change in both cell wall anisotropy and growth direction.

Dynamics of growth and tension

Prior to the reorientation of exocarp CMTs, *C. hirsuta* fruit are fully elongated but lack the tension required to explode.[2] Therefore, by switching the direction of cell wall reinforcement and growth, exocarp cells grow in width and acquire a more optimal shape to build contractile tension. But how is it possible that growth, a process that relaxes stress in the cell wall, generates more contractile tension in the valve?

To explore this apparent paradox, we performed FEM growth simulations using MorphoMechanX software (STAR Methods; Methods S1). We modeled growth as irreversible cell wall extension, also referred to as cell wall yielding or creep.[9] The amount of growth depends on the elastic strain on the cell wall, which is proportional to the stress resulting from turgor pressure.[22–25] The strain is then multiplied by an extensibility parameter to determine the growth of the elements.[22] When we added this growth model to cell file simulations with material anisotropy in the length direction, we found that maximal strain, and hence growth, was oriented in the width direction (Figure 4A; Video S4). This matches the growth we observed in cell width when the deposition of cellulose microfibrils was oriented to the length direction in exocarp cells (Figures 3D and 3E).

To investigate how this growth could lead to an increase in contractile tension, we designed a series of simulations with a file of cells geometrically comparable to exocarp cells starting growth in the width direction. Cell size was set to 50 × 26 × 10 μm (length, width, and depth), and other mechanical parameters were assigned that were identical to previous inflation simulations (Table S1). Turgor pressure remained constant[2] and cell wall extensibility was set uniformly. The simulation cycle consisted of (1) cell pressurization at a fixed value that is maintained throughout the simulation; (2) a growth step, in which elastic strain multiplied by extensibility was used to simulate yielding and grow the cell wall; and (3) recalculation and update of mechanical equilibrium (STAR Methods). Steps (2) and (3) were reiterated until cells reached a target width of 50 μm, which matches our measurements of mature exocarp cell width (Figures 1D and 3A). We fixed the ends of the cell file to mimic the constraint exerted on the growing exocarp tissue by its physical attachment to the rest of the fruit (Video S4).

We used these simulations to assess the effect of growth on contractile tension. To do this, we stopped the simulation at intermediate points and released the cell file ends. In this way, we could measure the stretch ratio between the length of the cell file with free versus fixed ends at intermediate growth steps in the process (Figure 4B). We tested two growth scenarios where we allowed almost none (Figures 4B and S3A), or some (Figure S3A), relaxation of cell wall stress in the stiffer, length direction. This was done by modulating the yield threshold of the cell wall, which has to be exceeded to activate growth[9]: a higher threshold of 0.1 in the first scenario and a lower threshold of 0.01 in the latter (STAR Methods; Methods S1). As the soft direction of the wall is stretched beyond both of these thresholds, the yield criterion will only significantly affect growth in the stiff direction. As cell width increased through growth from approximately 30 to 50 μm, we found that the stretch ratio of the cell file decreased from 0.93 to 0.89 when the yield threshold was low (Figure S3A; Table 1). At the higher yield threshold, the stretch ratio decreased even further to 0.84 (Figures 4B and S3A; Table 1). These results demonstrate that although growth is a stress-release process, the release of stress in the width direction can increase stress in the length direction by changing cell geometry and increasing the stress associated with a larger cell surface area. This requires that the relaxation of wall stress in the length direction is inhibited, in this case by significant reinforcement of cellulose microfibrils in that direction, which reduces the strain below the yield threshold.

In summary, the stretch ratio of 0.84 obtained for a simulated file of growing cells (Figure 4B; Table 1) is comparable to the empirical value of 0.8 reported previously.[2] Therefore, material anisotropy, specified as longitudinally aligned fiber reinforcement, combined with turgor-driven growth and limited relaxation in the fiber direction, can explain the generation of contractility as a file of cells grows in width.

A cross-lamellate pattern of cellulose microfibrils enhances contractility

CMT arrays are dynamic and can reorganize within a scale of minutes,[26,27] and these arrays guide only the most recently added layer of cellulose microfibrils in the cell wall. This leads to a degree of heterogeneity in microfibril orientation and contributes to a cross-lamellate pattern between different cell wall layers.[28–30] This type of pattern was observed in mature exocarp cells of *C. hirsuta* fruit where longitudinally aligned cellulose

Please cite this article in press as: Mosca et al., Growth and tension in explosive fruit, Current Biology (2024), https://doi.org/10.1016/j.cub.2024.01.059

CellPress
OPEN ACCESS

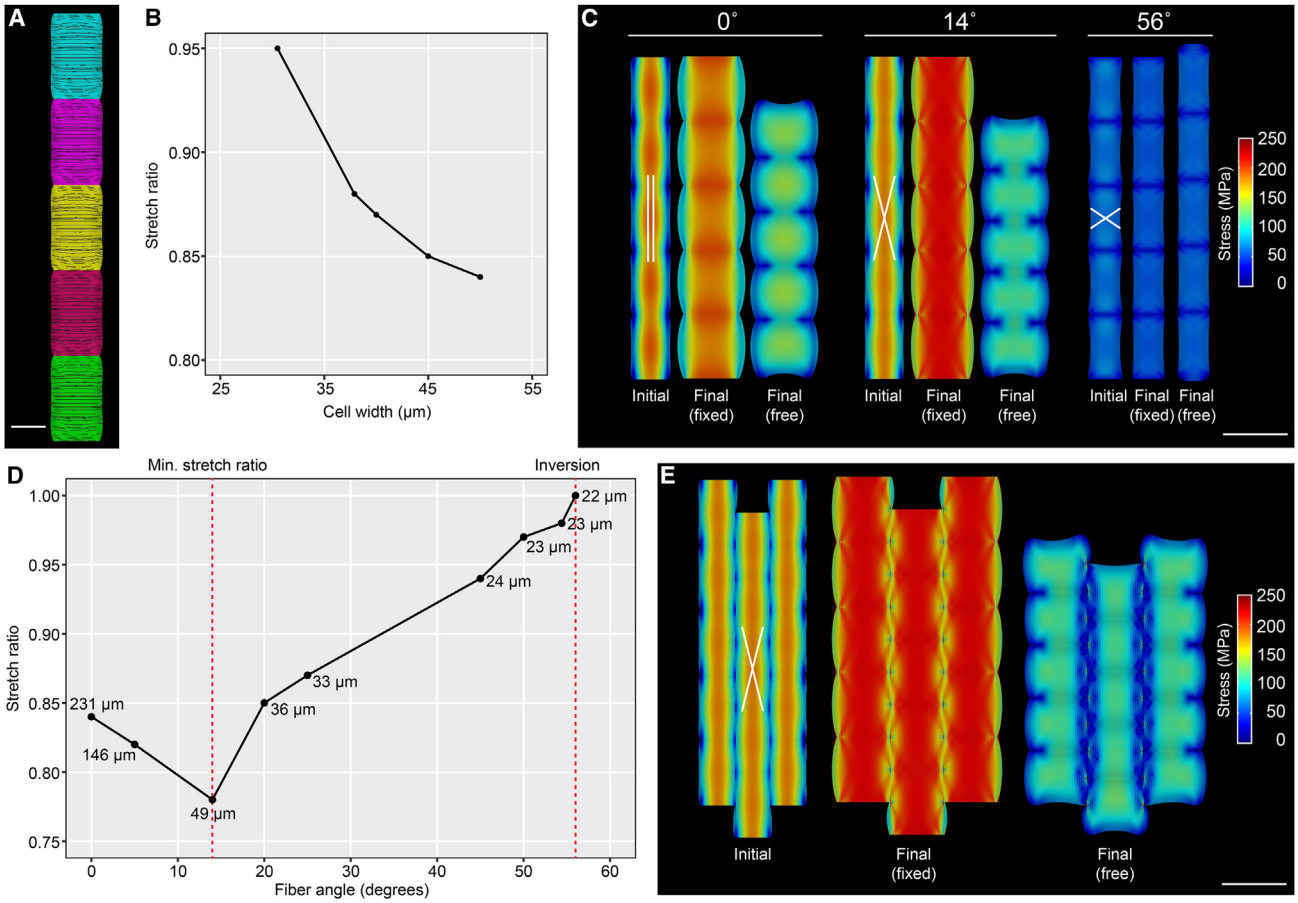

Figure 4. Interaction of growth and cell wall anisotropy determines cell length contraction

All FEM growth simulations performed in MorphoMechanX using cell templates of dimensions 50 × 26 × 10 μm (length × width × depth) inflated to 0.7 MPa.

(A and B) Strain-based growth model comprising transversely isotropic material reinforced with longitudinal fibers of 4,000 MPa stiffness.

(A) Direction of maximal strain, and therefore main growth direction, indicated by black lines in a file of inflated cells before growth.

(B) Plot of stretch ratio (y axis), measured along the cell file length when ends are free versus fixed, at intermediate steps of the growth simulation as cell width (x axis) increases to a final target of 50 μm.

(C–E) Multi-layer growth model comprising an isotropic layer undergoing strain-based growth joined with two layers of stiff fibers (2,000 MPa each layer) that do not respond to growth. Fiber orientation in each of the two layers is indicated as white lines on initial cell file. Shown for each simulation: a file of inflated cells with fixed ends before growth starts (Initial), at the end of growth (Final, fixed), and once the ends of the cell file are released (Final, free).

(C) Length contraction and stress compared between three simulations with either 0°, 14°, or 56° fiber angles, with respect to vertical. Stress ratios: 0.84 (0°), 0.78 (14°), and 1.005 (56°).

(D) Plot of stretch ratio (y axis), measured along the cell file length when ends are free versus fixed, in simulations with different fiber angles (x axis) from 0° through to 56°. Stretch ratios computed at 50 μm cell width or maximal width if less than 50 μm. Maximal cell width achieved through growth is annotated on the plot for each simulation (shown in μm). Fiber angles of 14° (minimal stretch ratio) and 56° (inversion) are highlighted by red dashed lines.

(E) Growth simulation in a block of cells with 14° fiber angle. Stress increases during growth to a maximum cell width of 41.4 μm (compare Initial versus Final, fixed) and drops once the cell file ends are released (Final, free). Stretch ratio: 0.82. Heatmaps display trace of Cauchy stress tensor.

Scale bars, 20 μm (A) and 50 μm (C and E).

See also Figure S3 and Videos S4 and S5.

microfibrils are not parallel, but rather cross at acute angles.[2] For these reasons, we performed a new series of simulations to explore whether deviations from a parallel fiber orientation can affect the process of building contractility in growing exocarp cells.

To vary the orientation of fiber reinforcement in the cell wall, we designed a multi-layer model. The cell wall is treated as a continuum in all of our models, rather than an explicit description of discrete fibers. Therefore, we used multiple layers to ascribe distinct orientations of fiber reinforcement within a growing, composite material. This multi-layer model comprises an isotropic layer that grows and two different fiber-dominated layers, representing the averaged contribution of cellulose microfibrils oriented at distinct angles in each layer, which do not grow (Figure S3B). The anisotropic component of the previous growth model was essentially split between the two fiber-dominated layers (parameter details in Table S1). These fiber-dominated layers are prevented from growing due to the high density of oriented cellulose microfibrils, which, according to our previous results (Figure 4B), will not be able to stretch beyond the

Please cite this article in press as: Mosca et al., Growth and tension in explosive fruit, Current Biology (2024), https://doi.org/10.1016/j.cub.2024.01.059

Table 1. Summary of stretch ratios from FEM growth simulations

Growth model	Stretch ratio after inflation	Stretch ratio after growth
Transversely isotropic material, low strain threshold (0.01; Figure S3A)	0.93	0.89
Transversely isotropic material, high strain threshold (0.1; Figures 4B and S3A)	0.93	0.84
Multi-layer, cell file, 0° fiber angle (Figure 4C)	0.94	0.84
Multi-layer, cell file, 14° fiber angle (Figure 4C)	0.94	0.78
Multi-layer, cell file, 56° fiber angle (Figure 4C)	1	1.02
Multi-layer, cell block, 0° fiber angle (Figure S3F)	0.93	0.86
Multi-layer, cell block, 14° fiber angle (Figure 4E)	0.93	0.82

Stretch ratios measured along the cell file length for different growth model simulations after inflation (before growth) and after growth (when ends are free versus fixed). Stretch ratios were computed after growth achieved a target cell width of 50 μm or else the maximal cell width achieved if less than 50 μm. See also Figures 4 and S3.

yield threshold that initiates growth. Therefore, these two layers deform purely elastically. Only the isotropic layer undergoes irreversible expansive growth, which implies a change in its reference configuration and a relaxation of the accumulated tension in this layer.[9,22,23] The three layers are geometrically joined, meaning that their mesh nodes are shared, their displacement is unique, and the nodal forces moving the points toward their equilibrium configuration are computed as the sum of the forces provided by each layer (Figure S3B; Methods S1; STAR Methods). In this way, the three layers can be treated as a composite material.

In order to compare this multi-layer model with our previous growth model, we assigned a common fiber direction parallel to the longitudinal cell file in both fiber layers. Under a hypothesis of full compressibility (Poisson ratios equal to zero; Table S1), where the two modeling approaches are theoretically comparable, the multi-layer model produced the same stress pattern and deformation as the previous growth model (Figure S3E). We also tested the effect of imposing symmetry on the fiber angles in each layer. Comparable results were produced with asymmetric fiber angles, although the cell file twisted when its ends were released (Figure S3C). Therefore, symmetric angles allowed a simpler computation of stretch ratios.

We performed simulations with two symmetric families of fibers at increasing angles relative to the vertical direction (Figures 4C and 4D). We computed the stretch ratio at the end of the growth process when cells reached a target width of either 50 μm or the maximal width attained if less than 50 μm. As before, we calculated the stretch ratio by comparing the final cell file length with free versus fixed ends (Figures 4C and S2B). To test the effect of fiber angle on stretch ratio, we varied the angle from 0° up to 56° with respect to vertical (Figure 4D). We found that the stretch ratio reached a minimum around a fiber angle of 14° and then increased at angles above 14° (Figure 4D). An inversion in the stretch behavior was reached at 56° (Figures 4C and 4D; Table 1), in agreement with analytical predictions for a cylinder under pressure that is reinforced by two populations of fibers at symmetric angles to vertical.[31]

In simulations where the fiber angles were 0° or 14°, we found a large reduction in stress was associated with contraction of the final cell file once the ends were released (Figure 4C; Video S5). The stretch ratio was 0.84 when the fiber angle was 0° (Figures 4C and 4D; Table 1). This value is identical to the previous growth model, with a single layer of transversely anisotropic material properties, grown to 50 μm cell width (Figures 4B; Table 1), providing further evidence that the two modeling approaches are comparable. However, as the fiber angle changed from parallel to 14°, with respect to vertical, we found that the stretch ratio of the cell file decreased from 0.84 to 0.78 (Figures 4C and 4D; Table 1). Since both cell files had the same stretch ratio before growth (0.94; Table 1), this suggests that the higher contractility of the cells with crossed fibers (14°) is actively reached through growth.

The reason that fibers in a crossed pattern (14°) can achieve a lower stretch ratio lies in the additional tension exerted on the fibers during growth. The expansion in cell width due to growth of the isotropic layer exerts an additional elastic stretch on the fiber layers when the fibers are tilted rather than orthogonal to the direction of growth. This stretch in the direction of growth is transmitted along the tilted fiber direction and partially translated into additional pulling force (Figure S3D). Due to this interaction with growth, our findings suggest that crossed patterns of cellulose microfibrils can actually enhance the process of building contractile tension in growing exocarp cells.

Our findings also revealed the influence of increasing fiber angles on the maximum cell width achieved by growth. At fiber angles closest to parallel (0°), cells achieved the highest growth in width, and at angles from 14° and above, cells could no longer reach a width of 50 μm (Figure 4D). At these angles, the fibers restrict the amount of transverse strain generated for growth in width. Therefore, in our simulations, when fibers were crossed and offset at a slight angle to vertical, this limited the final cell width attained by growth, providing an intrinsic mechanism to halt the growth process.

To verify that our results are not limited to the simplified case of a single cell file, we implemented our multi-layer growth model in a block of cells that more realistically represents the growth of cells in the context of exocarp tissue (Figures 4E and S3F; STAR Methods). A large reduction in stress was associated with contraction of the cell block length once the ends were released after the growth process (Figures 4E and S3F). The stretch ratio of the central cell file in this block was 0.82 at a fiber angle of 14°, slightly higher than the ratio of 0.78 achieved in a single cell file (Table 1). The block configuration constrained the growth in width of these central cells such that they reached only 41.4 μm (Figure 4E). Even with this constraint, the stretch ratio of the central cell file with fibers offset at 14° (0.82; Figure 4E) was lower than a cell file with parallel fibers in a block

Please cite this article in press as: Mosca et al., Growth and tension in explosive fruit, Current Biology (2024), https://doi.org/10.1016/j.cub.2024.01.059

Table 2. Simulated exocarp pulling force

FEM simulation, cell template: width × length × depth (μm)	Final cell width (μm)	Stretch ratio	Exocarp pulling force (mN)
Crossed fibers (14° angle)			
Inflation, 26 × 50 × 10	29	0.94	35.6
Inflation, 45 × 50 × 10	50	0.84	44.0
Growth, 26 × 50 × 10	49	0.78	62.9
Parallel fibers (0° angle)			
Inflation, 26 × 50 × 10	29.4	0.94	32.4
Inflation, 45 × 50 × 10	50.6	0.85	44.1
Growth, 26 × 50 × 10	51.6	0.84	39.9

Force exerted at the ends of an exocarp cell layer after growth or inflation simulations. Final cell width, stretch ratio, and corresponding pulling force extrapolated from a cell file to a cell layer (valve width: 1 mm) are measured for the different multi-layer model templates indicated. Fiber angle in the multi-layer model is either crossed (14° angle) or parallel (0° angle) as indicated. Exocarp pulling force previously computed from extensometer experiments[2] for comparison: average = 37 mN, max = 75 mN.

configuration (0.86; Figure S3F) or as a single file (0.84; Figure 4C) (Table 1). Thus, our findings can be generally applied to a tissue context.

The stretch ratio is a simple and precise measure of the amount of contraction occurring in the exocarp both *in planta* and *in silico*. However, we were also interested in the force produced by exocarp contraction since this is fundamental to the explosive nature of seed dispersal in *C. hirsuta*. We previously used empirical extensometer experiments to measure the force required to extend coiled fruit valves, and then compute the force exerted by the exocarp layer before explosion.[2] To compare our simulations with these results, we computed the force exerted at the ends of a cell file and extrapolated this to the pulling force for the whole exocarp layer (valve width 1 mm; Table 2). Our results fell within the range of previously determined forces[2] (Table 2). We found that simple inflation simulations using tissue templates made of wider cells (~50 versus ~29 μm final cell width; Table 2) contracted more and produced more exocarp layer pulling force (Table 2). We found a similar increase in cell contraction and pulling force when cell width increased to ~50 μm, from an initial width of 26 μm, in growth simulations (Table 2). Interestingly, we found that growing cells with a crossed pattern of fibers, offset at 14°, produced the greatest pulling force (Table 2). This result indicates that if cells reach an optimal width through growth, they contract more and pull with greater force. This effect depends on the interaction of growth with crossed fibers. In fact, before growth onset, right after inflation, the pulling force and contractility are very similar for crossed and parallel fibers, and the difference increases only through growth (Tables 1 and 2; Figure S3D). In summary, our simulations show that growth actively generates more length contraction at the cell level and more pulling force at the tissue level, which contributes to the mean coiling velocity of the valve.

Cortical microtubules contribute to explosive valve coiling

Our findings predict that explosive valve coiling depends on exocarp CMTs, since these contribute to the orientation of cellulose microfibril synthesis in the cell wall and the consequent cellular growth pattern. To test this prediction, we performed microtubule perturbation experiments. Treating *C. hirsuta* fruit with the microtubule depolymerizing drug oryzalin resulted in non-explosive fruit where the valves failed to coil (Figure S4A). However, it was not possible to ascribe this effect exclusively to exocarp cells since microtubules were depolymerized in all cell types of the fruit in these experiments.

To achieve more precise spatial and temporal resolution, we used a genetic system to depolymerize microtubules via inducible expression of a truncated version of the atypical tubulin kinase PROPYZAMIDE-HYPERSENSITIVE 1 (PHS1ΔP).[32] We expressed PHS1ΔP in exocarp cells using an epidermal-specific promoter (*pML1::GR-LhG4/pOp6::PHS1ΔP:mCherry*) and verified that CMTs were depolymerized specifically in response to dexamethasone and only in epidermal layers of the fruit (Figures S4B and S4C). For example, the mechanically important endocarp *b* cell layer of the fruit valve was unaffected in these transgenic lines (Figure S4C). Using live confocal imaging of *pML1::LhGR>>PHS1ΔP:mCherry; p35S::GFP:TUA6* plants, we imaged exocarp cells in 7-mm-long fruit, immediately before and after dexamethasone treatment (48 h, 96 h, and 8 days; Figure 5). The initial alignment of exocarp CMTs was perpendicular to the long axis of the fruit (pre-induction; Figure 5A). Repeated dexamethasone treatment ensured that microtubule depolymerization was maintained throughout the time-lapse experiments (Figure 5A).

Following microtubule depolymerization, exocarp cell growth was slower and more isotropic (Figures 5B, S4D, and S4E). In particular, dexamethasone treatment significantly reduced the anisotropic growth in width observed in mock-treated fruit (96 h–8 days; Figures 5B, 5C, S4F, and S4G). To test whether cell wall anisotropy was also disrupted, we used osmotic treatments. Mature exocarp cells of dexamethasone-treated compared to mock-treated fruit contracted significantly less in length in response to increased turgor (Figures 5D and 5E). Thus, in the absence of CMTs to guide the orientation of newly deposited cellulose microfibrils, cell wall anisotropy was reduced.

Explosive valve coiling was also reduced by microtubule depolymerization. Exploded valves from dexamethasone-treated fruit coiled more loosely, with reduced curvature, compared to the tightly coiled valves from mock-treated fruit (Figures 5F and 5G). Thus, CMT arrays contribute to the patterns

Please cite this article in press as: Mosca et al., Growth and tension in explosive fruit, Current Biology (2024), https://doi.org/10.1016/j.cub.2024.01.059

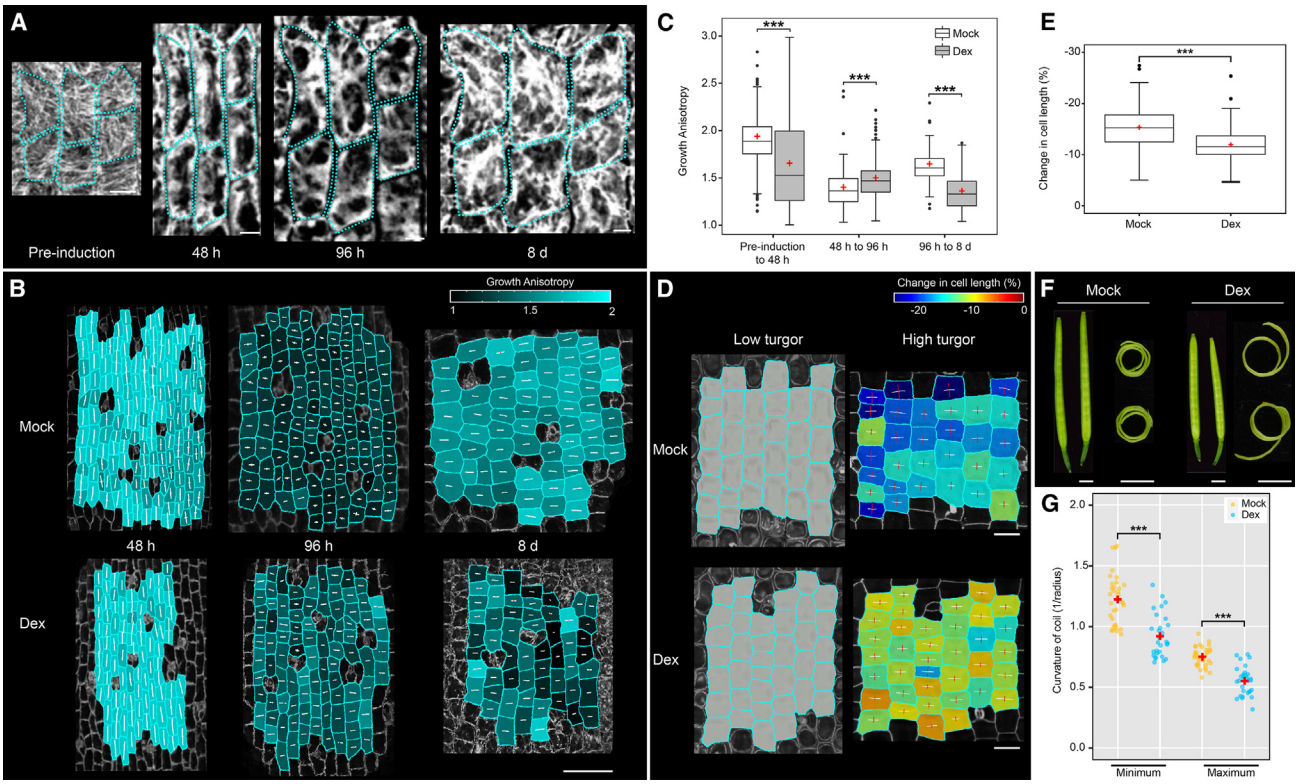

Figure 5. Cortical microtubules in fruit exocarp cells contribute to explosive valve coiling

Time-lapse confocal imaging of *C. hirsuta pML1::LhGR>>PHS1ΔP:mCherry; p35S::GFP:TUA6* exocarp cells during 8 days of fruit development starting with 7-mm-long fruit.

(A) CMT marker GFP-TUA6 immediately before (pre-induction) and 48 h, 96 h, and 8 days after dexamethasone treatment. Individual cells outlined in cyan.

(B and C) Growth anisotropy (ratio of PDG_{max} to PDG_{min}) between consecutive time points in mock- and dexamethasone-treated (Dex) fruit. Shown as heatmaps on second time point; white lines in each cell indicate the magnitude and direction of PDG_{max} (longer lines) and PDG_{min} (shorter lines) (B). Shown as boxplots (C), $n \geq 260$ cells from 4 fruit per time point (mock) and 262 cells from 5 fruit per time point (Dex).

(D and E) Osmotic treatment of mock- and dexamethasone-treated fruit. Percentage change in exocarp cell length, relative to the long axis of the fruit, in high turgor pressure (pure water) relative to low turgor pressure (1 M salt); shown as heatmaps, lines indicate expansion (white) or shrinkage (red) of cell dimensions (D), and boxplots (E), n = 195 cells from 4 fruit (mock) and 164 cells from 3 fruit (Dex).

(F and G) Mock- and dexamethasone-treated fruit and coiled valves, 11 days after treatment (F), and scatterplot showing minimum and maximum curvature of coiled valves (1/radius) (G), n = 35 valves (mock) and 31 valves (Dex). All plots indicate mean (red cross) and significant differences at ***$p < 0.001$ using a Wilcoxon signed-rank test or Student's t test.

Scale bars, 10 μm (A), 100 μm (B), 50 μm (D), and 1 mm (F).

See also Figure S4.

of cellular growth and cell wall anisotropy that determine exocarp cell contraction and underpin explosive valve coiling.

DISCUSSION

Exploding seed pods in *C. hirsuta* harness properties of cellular growth to generate tension. We identified a key role for CMTs in this process. A switch in microtubule alignment reorients the direction of cellulose microfibril synthesis in the wall, changing growth direction and consequently cell shape. The large, square faces of these cells, reinforced by aligned cellulose microfibrils, bulge out in response to turgor pressure and pull in the length direction. This puts the outer exocarp layer of the fruit valve under tension and the lignified inner layer under compression, resulting in the build-up and storage of potential elastic energy that powers explosive seed dispersal. Thus, by combining computational modeling with biological experiments, we could explain how specific cellular features cause the tissue-level mechanics underpinning explosive dispersal.

Cell geometry plays a key role in explaining how growth, which is a stress relaxation process, can generate tension. Exocarp cells initially grow by elongating, but later in fruit development they switch to grow in width. As they widen, the outer and inner faces of these relatively shallow cells become large and square, causing mechanical stress to accumulate as they bulge out. Therefore, although growth is a stress-release process, growth in the width direction actually increases stress in the length direction and generates pulling force. For this to work, it is important that the cell wall resists yielding in the longitudinal direction, which is reinforced by aligned cellulose microfibrils, in order not to lose its longitudinal elastic tension under the action of growth.

A second mechanism, which acts in concert with cell shape, is the cross-lamellate pattern of cellulose microfibrils in the cell

Please cite this article in press as: Mosca et al., Growth and tension in explosive fruit, Current Biology (2024), https://doi.org/10.1016/j.cub.2024.01.059

wall. Growth in the width direction exerts an extra stretch on the fibers, making them pull harder in the length direction (Figure S3D). In this way, growth becomes an active element that increases contractility beyond just the effect on cell geometry. As such, the exocarp behaves as a novel analog of a McKibben actuator, using growth to enhance the pulling force. This observation has potential applications in the field of biomimetics in connection with soft-actuator design. A similar mechanism based on cross-lamellate patterns of cellulose has been proposed for the formation of reaction wood.[33]

A key developmental event during exocarp cell growth is the switch in microtubule orientation. CMTs often align with the direction of maximal tension in plant tissues[34–38] and have been proposed to spontaneously orient with the direction of maximal tensile stress.[39] However, in fruit exocarp cells, microtubules reorient to align with the direction of minimal rather than maximal tensile stress. Based on both the geometry and cell wall anisotropy of exocarp cells prior to microtubule reorientation, maximal tensile stress is predicted to be oriented in the transverse direction.[9,23] Yet microtubules reorient to the longitudinal direction, suggesting that a developmental signal may dominate other proposed mechanisms, such as stress sensing, to orient microtubules in these cells. Identifying such a signal and understanding how exocarp microtubules switch orientation will be an important follow-up to this study.

Different perturbations showed that CMTs contribute to cell wall and growth anisotropy, and ultimately to explosive coiling of the fruit valves. Oryzalin treatment abolished explosive valve coiling, but it also disrupted secondary cell wall patterning in the endocarp *b* cell layer of the valves, which is known to be critical for explosive coiling.[2] On the other hand, tissue-specific perturbation may have underestimated the full role of microtubules in the exocarp, since growth of the exocarp cell layer is constrained by its physical attachment to underlying tissues, meaning it is not free to grow fully isotropically in response to microtubule depolymerization. Generating mutant alleles in *C. hirsuta* for known microtubule regulators will allow different types of perturbations that should further inform this question.

Our experiments underscore the importance of visualizing both CMTs and CESA proteins in different cell types and at different stages of development. For example, we observed that CESA3 particles were lost from the plasma membrane of exocarp cells soon after the last time point in our experiments, while CMTs remained well aligned. Therefore, CMT alignment cannot always be assumed to indicate active cellulose microfibril synthesis. In addition, the highly correlated orientation of CMTs and CESA3 trajectories in exocarp cells does not exclude the presence of aligned CESA3 trajectories in CMT-free domains.[13,14] For example, it may be interesting to investigate whether CMT guidance of CESA3 trajectories contributes more to the process of reorienting in response to developmental cues than to maintaining aligned trajectories during exocarp cell growth.

Our simulations indicate that a cross-lamellate pattern of cellulose microfibrils can enhance the active contraction of growing exocarp cells. Although it might have been possible to address this question using a classical modeling approach with two families of fibers,[40] the multi-layer formulation that we designed here has several advantages, including (1) the intuitive meaning of mechanical parameters assigned to each layer, (2) the ability to prescribe individual growth rules to each layer, and (3) computational ease. For example, it is possible to extend the model to any number of layers without additional complexity or significant computational cost. For these reasons, we suggest that this type of multi-layer modeling approach has potential applications beyond the scope of this study. For example, it opens up exciting possibilities to model the mechanics of plant cell walls,[41] including the formation of reaction wood that is thought to be driven by cross-lamellate patterns of cellulose.[33] By discriminating newly deposited layers in the cell wall from progressively aging layers, it allows testable hypotheses to be formulated about the differential contribution of these layers to cell mechanics, growth, and morphogenesis.

In summary, exocarp cells harness mechanical forces associated with turgor-driven growth to contract and generate tension in exploding seed pods of *C. hirsuta*. This illustrates how a novel mechanical trait can emerge from tinkering with existing cellular components during evolution.[42]

STAR★METHODS

Detailed methods are provided in the online version of this paper and include the following:

- KEY RESOURCES TABLE
- RESOURCE AVAILABILITY
  - Lead Contact
  - Materials availability
  - Data and code availability
- EXPERIMENTAL MODEL AND SUBJECT DETAILS
  - Plant materials and growth conditions
- METHOD DETAILS
  - Generation of transgenic lines
  - Microscopy and quantitative image analysis
- QUANTIFICATION AND STATISTICAL ANALYSIS
  - Computational FEM simulations

SUPPLEMENTAL INFORMATION

Supplemental information can be found online at https://doi.org/10.1016/j.cub.2024.01.059.

ACKNOWLEDGMENTS

We thank A. Emonet for graphic designs, M. Majda for preliminary observations, D. Moulton and M. Tsiantis for comments, A. Sampathkumar and A. Maizel for sharing plasmids, W. Faigl for plasmid construction, and L. Rambaud-Lavigne for assistance in characterizing transgenic lines. This work was supported by Deutsche Forschungsgemeinschaft FOR2581 Plant Morphodynamics grants to A.H. and R.S.S. and support from the University of Zurich Forschungskredit to G.M. We gratefully acknowledge support from a Max Planck Society core grant to the Department of Comparative Development and Genetics.

AUTHOR CONTRIBUTIONS

Conceptualization, A.H., R.S.S., and G.M.; investigation, G.M., R.C.E., L.B., and G.W.; initial investigation, M.A. and S.Y.; software, G.M. and B.L.; writing, A.H. and G.M. with input from R.S.S. and R.C.E.; funding acquisition, A.H. and R.S.S.; supervision, A.H. and R.S.S.

DECLARATION OF INTERESTS

The authors declare no competing interests.

Received: June 17, 2023
Revised: November 30, 2023
Accepted: January 24, 2024
Published: February 14, 2024

REFERENCES

1. Cummins, C., Seale, M., Macente, A., Certini, D., Mastropaolo, E., Viola, I.M., and Nakayama, N. (2018). A separated vortex ring underlies the flight of the dandelion. Nature *562*, 414–418. https://doi.org/10.1038/s41586-018-0604-2.
2. Hofhuis, H., Moulton, D., Lessinnes, T., Routier-Kierzkowska, A.L., Bomphrey, R.J., Mosca, G., Reinhardt, H., Sarchet, P., Gan, X., Tsiantis, M., et al. (2016). Morphomechanical innovation drives explosive seed dispersal. Cell *166*, 222–233. https://doi.org/10.1016/j.cell.2016.05.002.
3. Pérez-Antón, M., Schneider, I., Kroll, P., Hofhuis, H., Metzger, S., Pauly, M., and Hay, A. (2022). Explosive seed dispersal depends on SPL7 to ensure sufficient copper for localized lignin deposition via laccases. Proc. Natl. Acad. Sci. USA *119*, e2202287119. https://doi.org/10.1073/pnas.2202287119.
4. Zeiger, E., Farquhar, G.D., and Cowan, I.R. (1987). Stomatal Function (Stanford University Press).
5. Sleboda, D.A., Geitmann, A., and Sharif-Naeini, R. (2023). Multiscale structural anisotropy steers plant organ actuation. Curr. Biol. *33*, 639–646.e3. https://doi.org/10.1016/j.cub.2022.12.013.
6. McQueen-Mason, S., Durachko, D.M., and Cosgrove, D.J. (1992). Two endogenous proteins that induce cell wall extension in plants. Plant Cell *4*, 1425–1433. https://doi.org/10.1105/tpc.4.11.1425.
7. Cosgrove, D.J. (1997). Relaxation in a high-stress environment: the molecular bases of extensible cell walls and cell enlargement. Plant Cell *9*, 1031–1041. https://doi.org/10.1105/tpc.9.7.1031.
8. Cosgrove, D.J. (2022). Building an extensible cell wall. Plant Physiol. *189*, 1246–1277. https://doi.org/10.1093/plphys/kiac184.
9. Coen, E., and Cosgrove, D.J. (2023). The mechanics of plant morphogenesis. Science *379*, eade8055. https://doi.org/10.1126/science.ade8055.
10. McFarlane, H.E., Döring, A., and Persson, S. (2014). The cell biology of cellulose synthesis. Annu. Rev. Plant Biol. *65*, 69–94. https://doi.org/10.1146/annurev-arplant-050213-040240.
11. Paredez, A.R., Somerville, C.R., and Ehrhardt, D.W. (2006). Visualization of cellulose synthase demonstrates functional association with microtubules. Science *312*, 1491–1495. https://doi.org/10.1126/science.1126551.
12. Gutierrez, R., Lindeboom, J.J., Paredez, A.R., Emons, A.M.C., and Ehrhardt, D.W. (2009). Arabidopsis cortical microtubules position cellulose synthase delivery to the plasma membrane and interact with cellulose synthase trafficking compartments. Nat. Cell Biol. *11*, 797–806. https://doi.org/10.1038/ncb1886.
13. Fujita, M., Himmelspach, R., Hocart, C.H., Williamson, R.E., Mansfield, S.D., and Wasteneys, G.O. (2011). Cortical microtubules optimize cell-wall crystallinity to drive unidirectional growth in Arabidopsis. Plant J. *66*, 915–928. https://doi.org/10.1111/j.1365-313X.2011.04552.x.
14. Chan, J., and Coen, E. (2020). Interaction between autonomous and microtubule guidance systems controls cellulose synthase trajectories. Curr. Biol. *30*, 941–947.e2. https://doi.org/10.1016/j.cub.2019.12.066.
15. Green, P.B. (1962). Mechanism for plant cellular morphogenesis. Science *138*, 1404–1405. https://doi.org/10.1126/science.138.3548.1404.
16. Baskin, T.I. (2001). On the alignment of cellulose microfibrils by cortical microtubules: a review and a model. Protoplasma *215*, 150–171. https://doi.org/10.1007/BF01280311.
17. Ripoll, J.J., Zhu, M., Brocke, S., Hon, C.T., Yanofsky, M.F., Boudaoud, A., and Roeder, A.H.K. (2019). Growth dynamics of the Arabidopsis fruit is mediated by cell expansion. Proc. Natl. Acad. Sci. USA *116*, 25333–25342. https://doi.org/10.1073/pnas.1914096116.
18. Galstyan, A., Sarchet, P., Campos-Martin, R., Adibi, M., Nikolov, L.A., Pérez Antón, M., Rambaud-Lavigne, L., Gan, X., and Hay, A. (2021). INDEHISCENT regulates explosive seed dispersal. Preprint at bioRxiv. https://doi.org/10.1101/2021.06.11.448014.
19. Sapala, A., Runions, A., Routier-Kierzkowska, A.L., Das Gupta, M., Hong, L., Hofhuis, H., Verger, S., Mosca, G., Li, C.B., Hay, A., et al. (2018). Why plants make puzzle cells, and how their shape emerges. eLife *7*, e32794. https://doi.org/10.7554/eLife.32794.
20. Cheng, X., Lang, I., Adeniji, O.S., and Griffing, L. (2017). Plasmolysis-deplasmolysis causes changes in endoplasmic reticulum form, movement, flow, and cytoskeletal association. J. Exp. Bot. *68*, 4075–4087. https://doi.org/10.1093/jxb/erx243.
21. Strauss, S., Runions, A., Lane, B., Eschweiler, D., Bajpai, N., Trozzi, N., Routier-Kierzkowska, A.L., Yoshida, S., Rodrigues da Silveira, S., Vijayan, A., et al. (2022). Using positional information to provide context for biological image analysis with MorphoGraphX 2.0. eLife *11*, e72601. https://doi.org/10.7554/eLife.72601.
22. Bassel, G.W., Stamm, P., Mosca, G., Barbier de Reuille, P., Gibbs, D.J., Winter, R., Janka, A., Holdsworth, M.J., and Smith, R.S. (2014). Mechanical constraints imposed by 3D cellular geometry and arrangement modulate growth patterns in the Arabidopsis embryo. Proc. Natl. Acad. Sci. USA *111*, 8685–8690. https://doi.org/10.1073/pnas.1404616111.
23. Geitmann, A., and Ortega, J.K.E. (2009). Mechanics and modeling of plant cell growth. Trends Plant Sci. *14*, 467–478. https://doi.org/10.1016/j.tplants.2009.07.006.
24. Lockhart, J.A. (1965). An analysis of irreversible plant cell elongation. J. Theor. Biol. *8*, 264–275.
25. Zhao, F., Du, F., Oliveri, H., Zhou, L., Ali, O., Chen, W., Feng, S., Wang, Q., Lü, S., Long, M., et al. (2020). Microtubule-mediated wall anisotropy contributes to leaf blade flattening. Curr. Biol. *30*, 3972–3985.e6. https://doi.org/10.1016/j.cub.2020.07.076.
26. Chan, J., Calder, G., Fox, S., and Lloyd, C. (2007). Cortical microtubule arrays undergo rotary movements in Arabidopsis hypocotyl epidermal cells. Nat. Cell Biol. *9*, 171–175. https://doi.org/10.1038/ncb1533.
27. Eng, R.C., Schneider, R., Matz, T.W., Carter, R., Ehrhardt, D.W., Jönsson, H., Nikoloski, Z., and Sampathkumar, A. (2021). KATANIN and CLASP function at different spatial scales to mediate microtubule response to mechanical stress in Arabidopsis cotyledons. Curr. Biol. *31*, 3262–3274.e6. https://doi.org/10.1016/j.cub.2021.05.019.
28. Nicolas, W.J., Fäßler, F., Dutka, P., Schur, F.K.M., Jensen, G., and Meyerowitz, E. (2022). Cryo-electron tomography of the onion cell wall shows bimodally oriented cellulose fibers and reticulated homogalacturonan networks. Curr. Biol. *32*, 2375–2389.e6. https://doi.org/10.1016/j.cub.2022.04.024.
29. Xin, X., Lei, L., Zheng, Y., Zhang, T., Pingali, S.V., O'Neill, H., Cosgrove, D.J., Li, S., and Gu, Y. (2020). Cellulose synthase interactive1- and microtubule-dependent cell wall architecture is required for acid growth in Arabidopsis hypocotyls. J. Exp. Bot. *71*, 2982–2994. https://doi.org/10.1093/jxb/eraa063.
30. Zhang, T., Zheng, Y., and Cosgrove, D.J. (2016). Spatial organization of cellulose microfibrils and matrix polysaccharides in primary plant cell walls as imaged by multichannel atomic force microscopy. Plant J. *85*, 179–192. https://doi.org/10.1111/tpj.13102.
31. Goriely, A., and Tabor, M. (2013). Rotation, inversion and perversion in anisotropic elastic cylindrical tubes and membranes. Proc. Math. Phys. Eng. Sci. *469*, 20130011. https://doi.org/10.1098/rspa.2013.0011.
32. Fujita, S., Pytela, J., Hotta, T., Kato, T., Hamada, T., Akamatsu, R., Ishida, Y., Kutsuna, N., Hasezawa, S., Nomura, Y., et al. (2013). An atypical tubulin kinase mediates stress-induced microtubule depolymerization in Arabidopsis. Curr. Biol. *23*, 1969–1978. https://doi.org/10.1016/j.cub.2013.08.006.

33. Goswami, L., Dunlop, J.W.C., Jungnikl, K., Eder, M., Gierlinger, N., Coutand, C., Jeronimidis, G., Fratzl, P., and Burgert, I. (2008). Stress generation in the tension wood of poplar is based on the lateral swelling power of the G-layer. Plant J. *56*, 531–538. https://doi.org/10.1111/j.1365-313X.2008.03617.x.

34. Hejnowicz, Z., Rusin, A., and Rusin, T. (2000). Tensile tissue stress affects the orientation of cortical microtubules in the epidermis of sunflower hypocotyl. J. Plant Growth Regul. *19*, 31–44. https://doi.org/10.1007/s003440000005.

35. Hamant, O., Heisler, M.G., Jönsson, H., Krupinski, P., Uyttewaal, M., Bokov, P., Corson, F., Sahlin, P., Boudaoud, A., Meyerowitz, E.M., et al. (2008). Developmental patterning by mechanical signals in Arabidopsis. Science *322*, 1650–1655. https://doi.org/10.1126/science.1165594.

36. Sampathkumar, A., Krupinski, P., Wightman, R., Milani, P., Berquand, A., Boudaoud, A., Hamant, O., Jönsson, H., and Meyerowitz, E.M. (2014). Subcellular and supracellular mechanical stress prescribes cytoskeleton behavior in Arabidopsis cotyledon pavement cells. eLife *3*, e01967. https://doi.org/10.7554/eLife.01967.

37. Robinson, S., and Kuhlemeier, C. (2018). Global compression reorients cortical microtubules in arabidopsis hypocotyl epidermis and promotes growth. Curr. Biol. *28*, 1794–1802.e2. https://doi.org/10.1016/j.cub.2018.04.028.

38. Verger, S., Long, Y., Boudaoud, A., and Hamant, O. (2018). A tension-adhesion feedback loop in plant epidermis. eLife *7*, e34460. https://doi.org/10.7554/eLife.34460.

39. Hamant, O., Inoue, D., Bouchez, D., Dumais, J., and Mjolsness, E. (2019). Are microtubules tension sensors? Nat. Commun. *10*, 2360. https://doi.org/10.1038/s41467-019-10207-y.

40. Holzapfel, G.A., Stadler, M., and Schulze-Bauer, C.A.J. (2002). A layer-specific three-dimensional model for the simulation of balloon angioplasty using magnetic resonance imaging and mechanical testing. Ann. Biomed. Eng. *30*, 753–767. https://doi.org/10.1114/1.1492812.

41. Zhang, Y., Yu, J., Wang, X., Durachko, D.M., Zhang, S., and Cosgrove, D.J. (2021). Molecular insights into the complex mechanics of plant epidermal cell walls. Science *372*, 706–711. https://doi.org/10.1126/science.abf2824.

42. Jacob, F. (1977). Evolution and tinkering. Science *196*, 1161–1166. https://doi.org/10.1126/science.860134.

43. Hay, A., and Tsiantis, M. (2006). The genetic basis for differences in leaf form between Arabidopsis thaliana and its wild relative Cardamine hirsuta. Nat. Genet. *38*, 942–947.

44. Lampropoulos, A., Sutikovic, Z., Wenzl, C., Maegele, I., Lohmann, J.U., and Forner, J. (2013). GreenGate—a novel, versatile, and efficient cloning system for plant transgenesis. PLoS One *8*, e83043. https://doi.org/10.1371/journal.pone.0083043.

45. Schürholz, A.K., López-Salmerón, V., Li, Z., Forner, J., Wenzl, C., Gaillochet, C., Augustin, S., Barro, A.V., Fuchs, M., Gebert, M., et al. (2018). A comprehensive toolkit for inducible, cell type-specific gene expression in Arabidopsis. Plant Physiol. *178*, 40–53. https://doi.org/10.1104/pp.18.00463.

46. Vilches Barro, A., Stöckle, D., Thellmann, M., Ruiz-Duarte, P., Bald, L., Louveaux, M., von Born, P., Denninger, P., Goh, T., Fukaki, H., et al. (2019). Cytoskeleton dynamics are necessary for early events of lateral root initiation in Arabidopsis. Curr. Biol. *29*, 2443–2454.e5. https://doi.org/10.1016/j.cub.2019.06.039.

47. Desprez, T., Juraniec, M., Crowell, E.F., Jouy, H., Pochylova, Z., Parcy, F., Höfte, H., Gonneau, M., and Vernhettes, S. (2007). Organization of cellulose synthase complexes involved in primary cell wall synthesis in Arabidopsis thaliana. Proc. Natl. Acad. Sci. USA *104*, 15572–15577. https://doi.org/10.1073/pnas.0706569104.

48. Barbier de Reuille, P., Routier-Kierzkowska, A.L., Kierzkowski, D., Bassel, G.W., Schüpbach, T., Tauriello, G., Bajpai, N., Strauss, S., Weber, A., Kiss, A., et al. (2015). MorphoGraphX: a platform for quantifying morphogenesis in 4D. eLife *4*, e05864. https://doi.org/10.7554/eLife.05864.

49. Schindelin, J., Arganda-Carreras, I., Frise, E., Kaynig, V., Longair, M., Pietzsch, T., Preibisch, S., Rueden, C., Saalfeld, S., Schmid, B., et al. (2012). Fiji: an open-source platform for biological-image analysis. Nat. Methods *9*, 676–682. https://doi.org/10.1038/nmeth.2019.

50. Boudaoud, A., Burian, A., Borowska-Wykręt, D., Uyttewaal, M., Wrzalik, R., Kwiatkowska, D., and Hamant, O. (2014). FibrilTool, an ImageJ plug-in to quantify fibrillar structures in raw microscopy images. Nat. Protoc. *9*, 457–463. https://doi.org/10.1038/nprot.2014.024.

51. R Core Team (2019). R: A language and environment for statistical computing (R Foundation for Statistical Computing).

52. Chapelle, D., and Bathe, K.-J. (2011). The Finite Element Analysis of Shells - Fundamentals (Springer Berlin). https://doi.org/10.1007/978-3-642-16408-8.

53. Golub, G.H., and Van Loan, C.F. (1996). Matrix Computations (Johns Hopkins University Press).

54. Press, W.H., Teukolsky, S.A., Vetterling, W.T., and Flannery, B.P. (2007). Numerical Recipes. The Art of Scientific Computing, 3rd Edition Edition (Cambridge University Press).

Please cite this article in press as: Mosca et al., Growth and tension in explosive fruit, Current Biology (2024), https://doi.org/10.1016/j.cub.2024.01.059

STAR★METHODS

KEY RESOURCES TABLE

REAGENT or RESOURCE	SOURCE	IDENTIFIER
Chemicals, peptides, and recombinant proteins		
Propidium iodide (PI)	Sigma-Aldrich	25535-16-4
Murashige and Skoog (MS) medium	Duchefa	M0222
Dexamethasone (water soluble)	Sigma-Aldrich	D2915-100MG
NaCl	Roth	231-598-3
Oryzalin	ChemService	N-12729-100MG
Experimental models: Organisms/strains		
A. thaliana: Col-0	NASC	N1093
C. hirsuta: Ox	Hay et al.[43]	N/A
C. hirsuta: pML1::LhGR>>PHS1ΔP:mCherry; 35S::GFP:TUA6	This study	N/A
C. hirsuta: pCESA3::GFP:CESA3; *pUbi10::mCherry:TUA6*	This study	N/A
Software and algorithms		
Fiji	N/A	https://fiji.sc/
MorphoGraphX	N/A	https://www.MorphoGraphX.org
MorphoMechanX	N/A	https://www.MorphoGraphX.org/MorphoMechanX
Inflation & growth models for MorphoMechanX	This study	https://doi.org/10.5281/zenodo.10492759
RStudio	Posit	https://posit.co/

RESOURCE AVAILABILITY

Lead Contact

Further information and requests for resources and reagents should be directed to and will be fulfilled by the Lead Contact, Angela Hay (hay@mpipz.mpg.de)

Materials availability

All materials are available upon request.

Data and code availability

- All data reported in this paper will be shared by the lead contact upon request.
- All original code, instructions and all templates to reproduce the computational simulations can be found here: https://doi.org/10.5281/zenodo.10492759.
- Any additional information required to reanalyze the data reported in this paper is available from the lead contact upon request.

EXPERIMENTAL MODEL AND SUBJECT DETAILS

Plant materials and growth conditions

Cardamine hirsuta (Ox), herbarium specimen voucher Hay 1 (OXF),[43] and *Arabidopsis thaliana* (Col-0) were used throughout this study. Plants grown on soil were cultivated in the greenhouse in long-day conditions (days: 20°C, 16 h; nights: 18°C, 8 h). Transgenic plants were generated by the floral dip method using *Agrobacterium tumefaciens*. *C. hirsuta p35S::GFP:TUA6* plants were described previously.[2]

METHOD DETAILS

Generation of transgenic lines

pML1::GR-LhG4/pOp6::PHS1ΔP:mCherry was generated as a multiple expression GreenGate cassette from two intermediary modules, built using previously described entry vectors[44–46] (PHS1ΔP, gift from A. Maizel; all other vectors, Addgene). Both modules were combined in pGGZwf01[3] and transformed into *C. hirsuta p35S::GFP:TUA6* plants.[2] Twenty-eight Basta-resistant lines were selected,

Please cite this article in press as: Mosca et al., Growth and tension in explosive fruit, Current Biology (2024), https://doi.org/10.1016/j.cub.2024.01.059

tested for dexamethasone induction, and transgene copy number determined (iDNA Genetics). *pUBIQUITIN10::mCherry:TUA6* was generated by *Not*I digest of pMT813 to release the expression cassette. The insert was blunted, ligated into *Sma*I-digested pPZP200-Basta binary vector, and transformed into *C. hirsuta* plants. Transgene copy number was determined (iDNA Genetics) for nine independent lines. A *pCESA3::GFP:CESA3* construct[47] (gift from A. Sampathkumar) was transformed into *C. hirsuta pUbi10::mCherry:TUA6* plants. Ten hyogromycin-resistant lines were selected, analyzed for GFP-CESA3 localization at the plasma membrane, and transgene copy number determined (iDNA Genetics). Representative lines for each construct were analyzed in the T3 generation.

Microscopy and quantitative image analysis

A Leica TCS SP8 was used for Confocal Laser Scanning Microscopy (CLSM) with a Nikon 20x water dipping objective (20x/0.95 water) or a Nikon 63x oil objective (63x/1.4 oil) and with the following excitation (ex) and emission (em) parameters (wavelength in nm): GFP ex: 488, em: 550-650 bandpass filter; mCherry and basic fuchsin ex: 561, em: 600-665 bandpass filter; PI ex: 461, em: 550-650 bandpass filter.

Time-lapse imaging and dexamethasone induction of pML1::LhGR>>PHS1ΔP:mCherry

C. hirsuta pML1::LhGR>>PHS1ΔP:mCherry;p35S::GFP:TUA6 fruit of 7 mm length were carefully taped to a glass slide, while still attached to the plant, and 0.6 μm z stack slices of GFP signal in exocarp cells were acquired by CLSM using a 20x/0.95 water dipping lens (0 h time-point, pre-induction). After imaging, plants were separated into treatment and mock groups and fruit were dipped for 10 s in a solution containing 0.02% Silwett L-77 with 1mM water-soluble dexamethasone (Sigma-Aldrich) (Dex) or without (Mock). Plants were returned to the greenhouse overnight and the same treatments repeated the following day. At the 48 h time-point, CLSM imaging of the same fruits was repeated. After imaging, treatment of the fruits was repeated, and plants were returned to the greenhouse. Treatment of fruits continued every 48 h and CLSM imaging of the same fruits was repeated at 96 h and 8 d time-points. A minimum of four fruit valve replicates were imaged throughout each time-lapse experiment. z stack images were loaded into MorphoGraphX and segmented using signal from the GFP channel.[48] Parent relations for each cell between successive time points were determined and heat maps displayed on the second of two time points. Microtubule orientation, growth anisotropy and all other cellular parameters were quantified using existing functions in MorphoGraphX.[48] The principal direction of growth was determined relative to the fruit long axis.

At the 96 h time-point, GFP-TUA6 signal in the endocarp *a* and *b* cell layers was imaged in detached valves from dex- and mock-treated fruit from the experiment. Whole valves were mounted in water between a glass slide and coverslip and 0.3 μm z stack slices of GFP signal were acquired by CLSM using a 25x/0.95 water dipping lens.

At the 11 d time-point, dex- and mock-treated fruit from the experiment were triggered to explode. The coiled valves were photographed and circles were fitted to the maximum and minimum curvature of each valve using Fiji.[49] The radius of each circle was measured and valve curvature was quantified as the reciprocal of the radius of curvature.

At the 11 d time-point, detached valves from dex- and mock-treated fruit from the experiment were also embedded in 5% agarose. 100-150 μm sections were cut with a Leica Vibratome VT1000 S, stained for lignin using ClearSee with 0.2% Basic Fuchsin as previously described,[3] and 0.5 μm z stack slices of Basic Fuchsin signal were acquired by CLSM using a 20x/0.95 water dipping lens.

Osmotic treatments

Valves were detached from stage 15 (7 mm length) or stage 17b (20-22 mm length) *C. hirsuta p35S::GFP:TUA6* fruit and incubated in 1 mg/mL propidium iodide (PI, Sigma-Aldrich) for 10 min. Valves were then rinsed in water, cut into smaller sections and adhered with silicone vacuum grease to a small Petri dish with the exocarp facing up, and covered with water. The Petri dish was moved to the CLSM stage and 0.6 μm z stack slices of PI signal were acquired, starting at the exocarp cell surface, by CLSM using a 20x/0.95 water dipping lens (high turgor). Water was then removed from the Petri dish, replaced with 1 M NaCl and valves were incubated for 60 min before imaging of the same cells was repeated (low turgor). Plasmolysis was verified by checking that microtubules were fully depolymerized. Six replicate experiments were performed. z stack images were loaded into MorphoGraphX and segmented using signal from the PI channel.[48] Parent relations for each cell between high and low turgor treatments were determined and heat maps displayed on high turgor images. The orientation and magnitude of PDG values were determined relative to the fruit long axis with existing functions in MorphoGraphX.[48] PDG values were calculated using the principal directions of stretch of the cell junctions on 2.5D meshes, projected locally onto a best fit plane for each cell. This method gives similar dimension measurements as a 2D mesh if the sample is relatively flat. Osmotic experiments using mock- and dexamethasone-treated fruit of *pML1::LhGR>>PHS1ΔP:mCherry;p35S::GFP:TUA6* plants were performed as described above. Four mock- and three dexamethasone-treated replicates were analyzed at 11 d post-induction.

GFP-CESA3 live imaging and analysis

Valves were detached from stage 15 (7 mm length), stage 16 (10-12 mm) or early stage 17a (17-19 mm) *C. hirsuta pCESA3::GFP-CESA3;pUbi10::mCherry:TUA6* fruit. These fruit stages match the 0 h, 48 h and 96 h timepoints in the timelapse experiment described above. Older fruit did not have GFP-CESA3 signal at the plasma membrane. Valves were cut into smaller sections, mounted in perfluoroperhydrophenanthrene (Sigma-Aldrich) between a glass slide and coverslip, and GFP and mCherry signals were acquired by CLSM using a 63x/1.4 oil immersion lens. A single z-slice was taken every 12 s for 30 time-frames. Live imaging was performed for a minimum of 34 cells at each fruit stage. These two-channel images were processed using Fiji.[49] The Stackreg function was used to correct for sample drift and then split into two separate channels. Samples were corrected using the Bleach Correction function followed by background subtraction (50 pixel rolling ball radius). An average projection of the time series was then taken. The brightness/contrast was adjusted for both channels to optimize for visualization and subsequent analyses.

Please cite this article in press as: Mosca et al., Growth and tension in explosive fruit, Current Biology (2024), https://doi.org/10.1016/j.cub.2024.01.059

Specifically, the GFP-CESA channel was adjusted to avoid intense signal derived from the Golgi vesicles in order to better visualize GFP-CESA3 at the plasma membrane. Images were rotated to ensure that the cell long axis is parallel to the fruit long axis. TUA6 and CESA3 trajectory orientations were measured using FibrilTool[50] and the angle between the orientation and fruit long axis was measured.

Oryzalin treatments

C. hirsuta p35S::GFP:TUA6 fruit of 7 mm length were dipped in 125 μM Oryzalin or mock solution (0.03% Silwet) for 10 min each day for 16 days. GFP-TUA6 was imaged by CLSM, as described above, to verify CMT depolymerization. Whole fruit and dehisced valves were photographed after 16 days.

QUANTIFICATION AND STATISTICAL ANALYSIS

The following statistical analyses were done with R Statistical Software: Shapiro-Wilks, Wilcoxon signed-rank, F-test, Student's *t*-test, Pearson's correlation. Graphs were produced using the ggplot2 package.[51] All statistical details of experiments can be found in figure legends, including the statistical tests used, exact value of n, what n represents, and the definition of center and dispersion measures.

Computational FEM simulations

All Finite Element Method simulations were performed within the MorphoMechanX framework (https://morphographx.org/), a modeling platform based on MorphoDynamX and evolved from MorphoGraphX (https://morphographx.org/). Simulation templates were created with the Cell Maker Plugin of MorphoDynamX by using the Block Cell Layers feature and editing a text file to adjust for the different cell templates (see https://doi.org/10.5281/zenodo.10492759 for detailed instructions and example files). The reference template consisted of a line of 5 cells connected in the length (y-axis) direction, each cell has the dimensions 26 × 50 × 10 μm in width (x axis), length (y-axis) and depth (z axis) respectively. All simulations used the aforementioned template, except where cell width or depth was varied (Figures 2E, 2F, and S2C), or in the cell block simulations where cells were arranged in a staggered 5 × 5×5 block of files (Figures 4E and S3F). Templates were all triangulated with a regular mesh where the elements biggest side is equal to 1 μm. When two cells share a face, this is not duplicated, instead the same mesh elements and nodes refer to both cells. All simulations use a membrane approximation to represent the cell wall, with plane stress and a zero transversal shear strain hypothesis (Kirchhoff-Love theory for membranes[52]). Specific material properties assigned are listed (Table S1).

Inflation simulations (Figures 2, S1A, and S2)

Before the inflation simulation, the ends of the cell file (anticlinal walls orthogonal to the y-axis and belonging to only one cell) are prevented from being able to move in the y-direction (Dirichlet boundary condition). Afterwards, the template is inflated and the Cauchy stress can be visualized. Given the fixed ends and the orientation of material anisotropy in simulations shown in Figures 2 and S2, the maximal Cauchy stress component coincides with the longitudinal stress (parallel to the y-axis in our template orientation), therefore, this can be visualized as well. To know the maximal stress orientation and magnitude of the Cauchy stress tensor, its eigenvectors and values have been computed using the GSL library, specifically the gsl_eigen_symmv function (https://www.gnu.org/software/gsl/doc/html/eigen.html), which works for real, symmetric matrices.[53]

Once the inflation process has reached convergence (see the following paragraph for the criterion used), the template ends are allowed to move in all space directions again, and contraction takes place. The stretch ratio is obtained by measuring the length (along y-axis) of the three central cells before inflation, and after the cell ends are released from any constraint (Figure S2B).

The inflation simulations use a Saint Venant-Kirchhoff transversely isotropic material (the material properties have rotational symmetry around a specific direction, which is the direction conferring anisotropy to the wall, and which can be interpreted as the one reinforced by fibers, even if the description is purely continuous here) and have been developed adopting the same mathematical formulation and computational scheme reported in Hofhuis et al.[2] There is a small difference for the convergence tolerance, which now requires the mean of average residual force norm and maximal residual force norm to both be below an assigned threshold (Table S1). Material anisotropy was assigned on the cell faces before inflation and growth as indicated (Figure S2A).

Single layer growth simulations (Figures 4A, 4B, S1B, and S3A)

These growth simulations use the same formulation for material description and elastic deformation reported for the inflation simulations (Table S1). Templates start with either a cell file block where each cell is 16 × 15 × 8 μm (Figure S1B) or a file of cells of sizes 26 × 50 × 10 μm (Figures 4A, 4B, and S3A) in width, length and depth respectively. The cell file ends are initially fixed in the y-direction as described for Figures 4A, 4B, and S3A, while ends are free for Figure S1B. After elastic equilibrium has been reached, an iterative growth process takes place (one step of growth, followed by mechanical equilibrium re-computation) until the template reaches a width of approximately 50 μm (Figures 4A, 4B, and S3A) or after 20 iterations (Figure S1B); during this process the cell file ends are kept fixed in the y-direction (Figures 4A, 4B, and S3A). Growth is occurring as a turgor-driven, strain-based relaxation of the reference configuration and acts only as a planar tensor in the element local coordinates (no in-thickness growth). Details about the mathematical formulation and its implementation in MorphoMechanX are provided (Methods S1). At the end of the growth phase, the cell-file ends, which were prevented from moving in the y-direction, are released, and the cell file is free to elastically contract (Figures 4A, 4B, and S3A); note that this step is not required in Figure S1B.

Please cite this article in press as: Mosca et al., Growth and tension in explosive fruit, Current Biology (2024), https://doi.org/10.1016/j.cub.2024.01.059

Multi-layer growth simulations (Figures 4C–4E and S3C–S3F)

Multi-layer growth simulations are conceptually identical to the simulations described in the previous section, with the difference that the material used to describe the cell wall is now comprised of three layers (Figure S3B). This means that each triangle element of the mesh is assigned three different reference configurations (identical at simulation start), three different material laws and three different growth rules, but share the same current configuration (given by the space coordinates of the triangle vertices, Methods S1).

Since membrane elements have a purely virtual thickness, each layer can be thought of as fully co-penetrating the others and vice-versa, without any notion of spatial hierarchy. While the current configuration is unique and shared with all the layers, MorphoMechanX enables the user to identify each layer in the GUI and assign to it its own reference configuration, material properties and growth rule. In the specific three-layer model used in this work, there are.

(1) Two layers with transversely isotropic Saint-Venant Kirchhoff material properties.[2] For each layer, the anisotropy direction **M** (Methods S1) was assigned at an angle γ with respect to the long axis of the cell file at the simulation start (y-axis in Figure S2A); this angle should not be confused with the angle α made by **M** with respect to the first triangle side in the reference configuration (Methods S1). For all simulations, but one case (Figure S3C), one fiber layer was displaced by an angle $+\gamma$, and the other by an angle $-\gamma$, with respect to the y-axis, so that the fibers make a symmetric crossed pattern. The stiff component of each of these layers has a Youngs modulus (E_{fiber}) equal to half the value assigned to the Youngs modulus of the stiff component in the single layer growth model. The soft component Youngs modulus (E_{iso}) is assigned to be extremely soft (Table S1), as its value should be negligible with respect to the stiffness of the isotropic layer. These two transversely isotropic layers are not undergoing any growth process, only purely elastic deformation.
(2) One isotropic layer with Sain-Venant Kirchhoff material properties. The Youngs modulus (E) of this layer has the same value as the soft component (E_{iso}) of the single layer growth model. This layer is undergoing turgor-driven, strain-based growth.

All three layers are assigned to be rather incompressible (Poisson ratio $v = 0.4$) and turgor pressure acts on one layer (it is irrelevant which one), as its mechanical effect in terms of deformation is then affecting equally all the layers since they share the same unique current configuration.

Computation of the elastic equilibrium for the multi-layer in MorphoMechanX. Given the current configuration (unique) of the mesh triangles, and each layer's reference triangle and material properties, the nodal reaction forces for each layer are computed as usual.[2] In the assembly of the force vector (Voigt notation), the nodal forces from the three layers are summed, the same holds for the "stiffness matrix" used in the semi-implicit Euler scheme,[54] whose entries are given by the derivative of the nodal forces with respect to a mesh node's virtual displacement (which means that the contribution of the different layers for the same two nodes involved in the computation is summed). For further details see Methods S1.

Computation of growth for the multi-layer in MorphoMechanX. As already mentioned, only the isotropic layer performs growth, and this is computed as explained above for single layer growth simulations (see also Methods S1). This means that only for this layer the reference configuration will change, while for the other two layers it will stay the same from the simulation start until the end.

A tutorial explaining how to set-up and run a growth simulation for the multi-layer models is provided (Video S6).

Sensitivity analysis simulations (Tables S2 and S3)

To assess the dependance of the contractility (both pulling force and stretch ratio) of the line of cells on the choice for material parameters related to cell wall stiffness (E_{iso} and E_{fiber}), we performed a sensitivity analysis for a line of 5 cells of initial dimensions 50 × 50 × 10 μm (length × width × depth) which undergo an inflation simulation (Table S2). To assess the sensitivity of pulling force and stretch ratio to varying the Poisson ratio, we performed FEM inflation simulations using cell templates with size before inflation: 50 × 50 × 10 μm (length × width × depth), and FEM growth simulations with parallel or crossed (14°) fibers using multi-layer model templates with size before inflation: 50 × 26 × 10 μm (length × width × depth) and grown to reach approximately 50 μm in width (Table S3).